1999-09-01

Simulations to predict the countermeasure effectiveness of using pyrophoric type packets deployed from TALD aircraft

Demestihas, Mihail

Monterey, California. Naval Postgraduate School

NAVAL POSTGRADUATE SCHOOL
Monterey, California

THESIS

SIMULATIONS TO PREDICT THE COUNTERMEASURE EFFECTIVENESS OF USING PYROPHORIC TYPE PACKETS DEPLOYED FROM TALD AIRCRAFT

by

Mihail Demestihas

September 1999

Thesis Advisor: Pieper, Ron
Co-Advisor: Robertson, R. Clark

Approved for public release; distribution is unlimited.

REPORT DOCUMENTATION PAGE

Form Approved
OMB No. 0704-0188

1. AGENCY USE ONLY *(Leave blank)*	2. REPORT DATE	3. REPORT TYPE AND DATES COVERED
	September 1999	Master's Thesis

4. TITLE AND SUBTITLE
SIMULATIONS TO PREDICT THE COUNTERMEASURE EFFECTIVENESS OF USING PYROPHORIC TYPE PACKETS DEPLOYED FROM TALD AIRCRAFT

5. FUNDING NUMBERS

6. AUTHOR(S)
Lt Mihail Demestihas, HN

7. PERFORMING ORGANIZATION NAME(S) AND ADDRESS(ES)
Naval Postgraduate School
Monterey, CA 93943-5000

8. PERFORMING ORGANIZATION REPORT NUMBER

9. SPONSORING / MONITORING AGENCY NAME(S) AND ADDRESS(ES)

10. SPONSORING / MONITORING AGENCY REPORT NUMBER

11. SUPPLEMENTARY NOTES
The views expressed in this thesis are those of the author and do not reflect the official policy or position of the Department of Defense or the U.S. Government.

12a. DISTRIBUTION / AVAILABILITY STATEMENT
Approved for public release; distribution unlimited.

12b. DISTRIBUTION CODE

13. ABSTRACT *(maximum 200 words)*

Manned aircraft that are intended for surveillance or to complete a bombing mission will very likely be engaged by surface to-air-missiles having guidance systems based on infrared (IR) technology. The objective of this study was to characterize via simulation the amount of "cover" that can be obtained by dropping from a pre-launched, unmanned tactical air launched decoy (TALD) a sequence of pyrophoric materials to create an IR cloud, analogous to the interference created by microwave chaff, that would protect the manned aircraft from the missile. The performance analysis is based on a simple reticle based model in which the two-dimensional (2D) image is reduced to either a composite signal, created by the aircraft, or a composite noise, created by the pyrophoric expandable. The analysis leads to a computer simulation model producing time and space dependent signal-to-noise ratios. It is demonstrated that the simulation model can answer questions such as how long the materials need to burn, how much intensity is needed, what wavelength range is most effective, which pyrophoric packets should be dropped, and how many. A visual model of the time dependent IR pyrophoric cloud has also been created.

14. SUBJECT TERMS	15. NUMBER OF PAGES
Pyrophoric, Flare, Infrared (IR)	116
	16. PRICE CODE

17. SECURITY CLASSIFICATION OF REPORT	18. SECURITY CLASSIFICATION OF THIS PAGE	19. SECURITY CLASSIFI- CATION OF ABSTRACT	20. LIMITATION OF ABSTRACT
Unclassified	Unclassified	Unclassified	UL

NSN 7540-01-280-5500

Standard Form 298 (Rev. 2-89)
Prescribed by ANSI Std. 239-18

Approved for public release; distribution is unlimited.

SIMULATIONS TO PREDICT THE COUNTERMEASURE EFFECTIVENESS OF USING PYROPHORIC TYPE PACKETS DEPLOYED FROM TALD AIRCRAFT

Mihail Demestihas
Lieutenant, Hellenic Navy
B.S., Hellenic Naval Academy, 1988

Submitted in partial fulfillment of the
requirements for the degree of

MASTER OF SCIENCE IN ELECTRICAL ENGINEERING

from the

NAVAL POSTGRADUATE SCHOOL
September 1999

ABSTRACT

Manned aircraft that are intended for surveillance or to complete a bombing mission will very likely be engaged by surface to-air-missiles having guidance systems based on infrared (IR) technology. The objective of this study was to characterize via simulation the amount of "cover" that can be obtained by dropping from a pre-launched, unmanned tactical air launched decoy (TALD) a sequence of pyrophoric materials to create an IR cloud, analogous to the interference created by microwave chaff, that would protect the manned aircraft from the missile. The performance analysis is based on a simple reticle based model in which the two-dimensional (2D) image is reduced to either a composite signal, created by the aircraft, or a composite noise, created by the pyrophoric expandable. The analysis leads to a computer simulation model producing time and space dependent signal-to-noise ratios. It is demonstrated that the simulation model can answer questions such as how long the materials need to burn, how much intensity is needed, what wavelength range is most effective, which pyrophoric packets should be dropped, and how many. A visual model of the time dependent IR pyrophoric cloud has also been created.

TABLE OF CONTENTS

ACKNOWLEDGEMENT

This thesis dedicated to Prof. Ron Pieper and R.Clark Robertson for their help and support. Also I would like to thank George Floros and Rosie Tsuda for their support.

I. INTRODUCTION

A. BACKGROUND

The most effective anti-aircraft weapon ever created to-date is the infrared (IR) guided missile. Since their introduction into operational use in the early 1950s, IR missiles have far exceeded the expectations their designers. The enabling technology for practical IR missiles came from WWII research on detector materials that could be used to fashion detectors sensitive in the IR bands. These initial materials were sensitive to radiation in the near-IR (1-2 micron wavelength) band. Over the last 20 years, advanced designs have taken advantage of better detector materials, moving the bandpass from the near-IR into the mid-IR (3-5 micron band), where engine plume provides a superior signal for all-aspect engagement. The three to five micron band also has less atmospheric attenuation and clutter factors.

The need to protect aircraft from attack by effective, easily launched IR homing missiles led to the development of pyrotechnic flares. The flare needs to have a jamming-to-signal (J/S) ratio of greater than one to one versus the protected aircraft's signature to lure a missile away from the aircraft. Since the observed surface area of the IR signature of the flare is quite small, a pyrotechnic flare has to operate at very high temperatures to match or exceed

the in-band aircraft signature. But high temperatures shift the wavelength, and we are forced by the laws of physics to increase the size of the flare to provide enough energy at the correct wavelength. The flare's intensity is presumed to rapidly rise to several orders of magnitude higher than that of the target signature and ignite near the target aircraft, inside the field of view (FOV) of missile's seeker.

B. APPROACH

In this thesis the amount of protection that can be obtained by dropping a sequence of pyrophoric materials to create an IR chaff cloud will be simulated. A simple scenario will be defined in which the packets are dropped from a pre-launched unmanned tactical air launched decoy (TALD), and the manned aircraft follows, at a later time, close to the same path as the decoy, taking advantage of the interfering effect created by the pyrophoric clouds.

The heat-seeking missile is assumed to be in a prelaunch status so that missile aero-dynamics are not part of this initial study. The imaging capability of the missile is assumed to be defined in terms of a definable number of pixels within the known field-of-view. Also assumed known is the detector sensitivity and detectivity over one or more bands of wavelengths. The image of the aircraft is defined in terms of a distribution of hot spots. Any interference provided by the IR signature of the TALD aircraft are

ignored. A visual model for expenditure of the IR chaff cloud is created. The sequence and timing for the dropping of the packets are assumed to be known. Also, both the speed of the manned aircraft and the decoy are assumed known.

The analysis of the problem can answer questions such as how long the materials need to burn, how much intensity is needed, what wavelength range and distribution are most effective, the rate at which pyrophoric packets should be dropped and how many, and lastly, quantitatively what kind of signal-to-noise ratio (S/N) deterioration can be extracted. The mathematical software **MATLAB** will be used to simulate the pyrophoric material, provide image snapshots in time of the pyrophoric material, and calculate the resulting S/N.

Some basic IR theory such as Plank's Law, Wien's Law, and the Stefan-Boltzmann Law, are reviewed in Chapter II. Radiometric definitions, atmospheric absorption, and general characteristics of the different types of IR detectors are also discussed in Chapter II. The design of the pyrophoric model is discussed in Chapter III. The design of the aircraft plume model is addressed in Chapter IV. The integration of the pyrophoric and plume model is discussed in Chapter V. The first part of the simulation code and some S/N curves are presented in Chapter VI. The second part of the simulation code and the pyrophoric and plume images are

presented in Chapter VII. The use of multiple pyrophoric expendables is discussed in Chapter VIII. Finally, conclusions from the study of the pyrophoric model and future enhancements in modeling are presented in Chapter IX. Also, in Appendix A, B and C is a brief description of the symbols and the quantities that are used during the analysis or in the simulation code, the MATLAB codes, and the mathematical derivations, respectively.

II. BACKGROUND

A. INTRODUCTION

In the year 1800, Sir William Herschel, the royal astronomer to the King of England, was conducting an experiment with a prism in sunlight. The prism spread the sun's rays into a spectrum from violet to red. Herschel placed a thermometer in the violet color and recorded the temperature. He moved the thermometer through the colors from blue to red and noticed that the temperature increased progressively. He then moved the thermometer beyond the red end of the visible region and the temperature continued to increase. Thus, he found energy beyond the red; this energy has come to be known as infrared (IR).

A portion of the electromagnetic spectrum is indicated in Figure 2.1. All electromagnetic radiation obeys similar laws of reflection, refraction, diffraction, and polarization. The velocity of propagation is the same for all. They differ from one another only in wavelength and frequency. The portion of the spectrum that includes the infrared is depicted in greater detail in the lower part of Figure 2.1, where the infrared region is bounded on the short-wavelength side by visible light and on the long-wavelength side by microwaves. It is convenient to subdivide the infrared region into several parts. There are no exact

designations for the separation of infrared bands. The most universally accepted designations today are as follows: visible light up to 3 um is designated near infrared (NIR), middle infrared (MIR) is from 3 to 6 um, and far infrared (FIR) is from 6 to 15 um. Beyond 15 um is the extreme infrared (XIR).

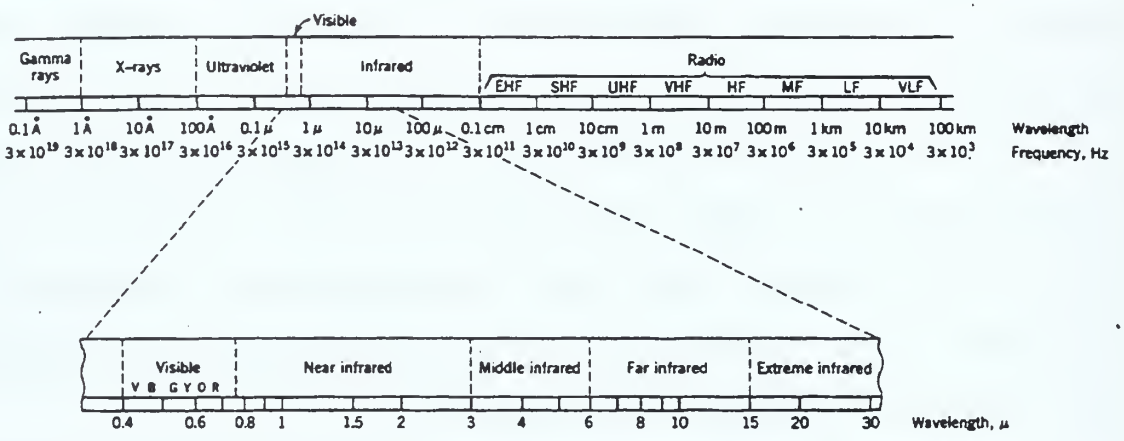

Figure 2.1 The Electromagnetic Spectrum. (From Ref [1])

B. RADIOMETRIC SYMBOLS

All objects with nonzero temperature will emit electromagnetic radiation. Some objects prove to be better radiators than others. The (hypothetical) best radiator is one that obeys a set of classical equations called the blackbody radiation equations. Some of terms used to describe IR sources and radiation are defined in Table 2.1.

Table 2.1 Symbols, Descriptions, and Units

Symbol	Term	Description	Unit
U	Radiant energy	Energy transferred by electromagnetic waves	Joule
P	Radiant flux	Rate of transfer of radiant energy	Watt(W)
W	Radiant emittance	Radiant flux emitted per unit area of a source	$W \cdot cm^{-2}$
J	Radiant intensity	Radiant flux per unit solid angle	$W \cdot cm^{-2}$
N	Radiance	Radiant flux per unit solid angle per unit area	$W \cdot cm^{-2}$
H	Irradiance	Radiant flux incident per unit area	$W \cdot cm^{-2}$
W_λ	Spectral radiant emittance	Radiant emittance per unit wavelength interval at a particular wavelength	$W \cdot cm^{-2}$
ε	Emissivity	Ratio of radiant emittance of a source to that of a blackbody at the same temperature	Dimensionless

C. BLACKBODY RADIATORS

The spectral density distribution of the power radiated into a hemisphere from a blackbody radiator per unit area of the source is given by Planck's Law [2]:

$$W_\lambda(\lambda,T)=\frac{2\pi hc^2}{\lambda^5}\frac{1}{\exp\left(hc/\lambda kT\right)-1}=\frac{c_1}{\lambda^5}\frac{1}{\exp\left(c_2/\lambda T\right)-1} \qquad (II-1)$$

where

- W_λ is the spectral radiant emittance of the source with units of $W\cdot cm^{-2}\cdot\mu m^{-1}$
- h is Planck's constant ($h=6.625\times10^{-34}$ joules·s)
- c is the vacuum velocity of light ($c=3\times10^{8}$ m·s^{-1})
- λ is the wavelength of the radiation (μm or nm)
- k is Boltzman's constant ($k=1.38\times10^{-23}$ joules·K^{-1})
- T is the temperature of the source in K
- $c_1= 2\pi hc^2=3.74\times10^{4}$ $W\cdot cm^{-2}\cdot\mu m^{4}$
- $c_2= hc/k=1.439\times10^{4}$ μm·K

Plots of the spectral radiant emittance for a typical range of temperatures encountered in our environment are shown in Figure 2.2. The spectral radiant emittance is the spectral power distribution normalized by the area of the source. Note that most of the energy is in the infrared portion of the spectrum. As the temperature of the source increases, we

note that the area under the curve increases, and the location of the peak shifts toward the shorter wavelengths.

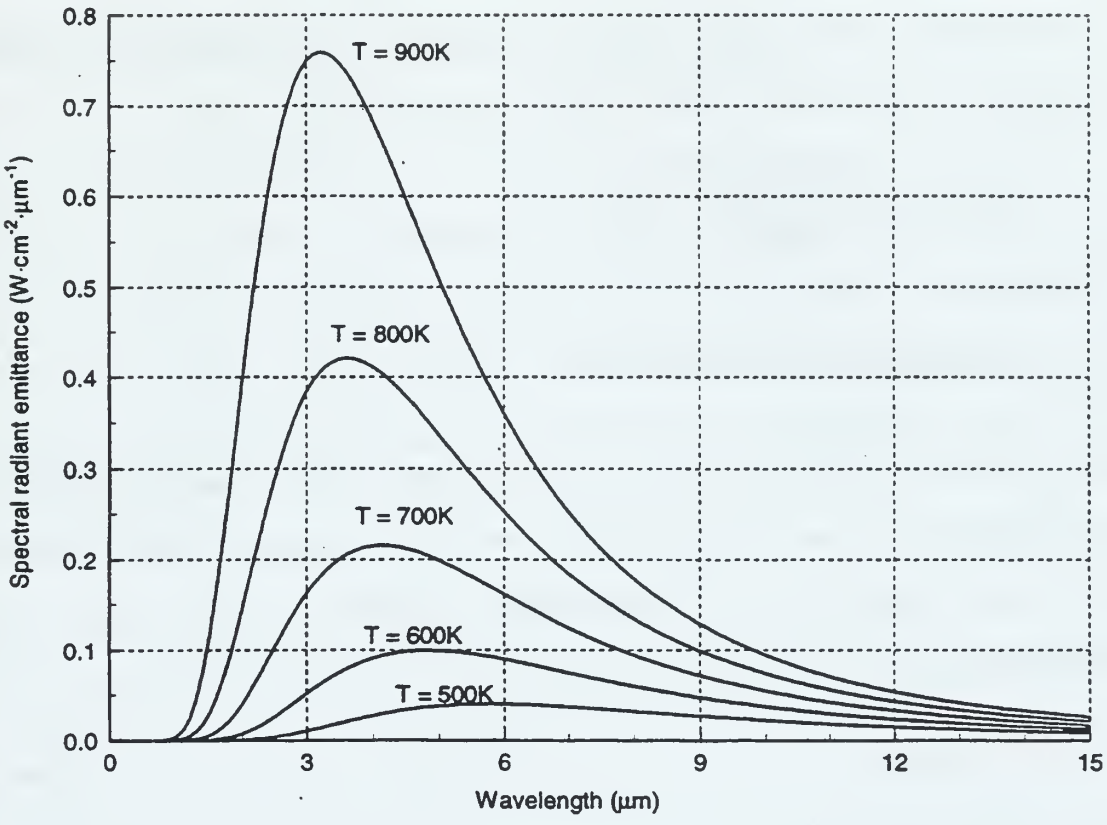

Figure 2.2 Spectral Radiant Emittance vs. Wavelength for Blackbodies of Various Temperatures. (From Ref [2])

The location of the peak of the spectral radiant emittance is found by taking the derivative of Planck's Law with respect to wavelength. It can be shown that the result gives *Wien's Law*, the wavelength of the peak spectral radiant emittance :

$$\lambda_m = \frac{2.896\times10^3}{T[K]} \quad [\mu m] \qquad (II-2)$$

Knowing the temperature of the source, we can calculate the location of the peak emittance and, as shown in Figure 2.2, higher temperatures imply lower λ_m.

The value of the peak spectral radiant emittance is found by substituting (II-2) into (II-1) to obtain

$$W_\lambda(\lambda_m, T) = \frac{21.2(2\pi hc^2)T^5}{\left(hc/k\right)^5} = bT^5 \qquad (II-3)$$

where

$$b = 1.286\times10^{-15} W\cdot cm^{-2}\cdot\mu m^{-1}\cdot K^{-5}.$$

The total emittance W is the total power emitted into a hemisphere at all wavelengths per unit area of the source. It is found by integrating Planck's Law over all wavelengths,

$$W = \int_0^\infty W_\lambda d\lambda \qquad (II-4)$$

The result of this integration is

$$W = \frac{2\pi^5 k^4 T^4}{15c^2h^3} = \sigma T^4 \qquad (II-5)$$

where

$$\sigma = 5.67\times10^{-12} W\cdot cm^{-2}\cdot{}^\circ K^{-4}$$

which represents the *Stefan-Boltzmann Law* and shows that the total power per unit area of the source increases as the fourth power of the temperature.

We frequently pass electromagnetic radiation through a spectral filter (like the atmosphere) with a spectral response of the form $S(\lambda)$. The emittance that is passed by such a filter is

$$W(\lambda_1,\lambda_2)=\int_{\lambda_1}^{\lambda_2} S(\lambda)W_\lambda d\lambda \qquad (II-6)$$

Figure 2.3 is an illustration of one such graph where the vertical axis is used to compute the fraction of the total emittance that lies between a wavelength of 0 μm and some upper wavelength divided by the total emittance over all wavelengths.

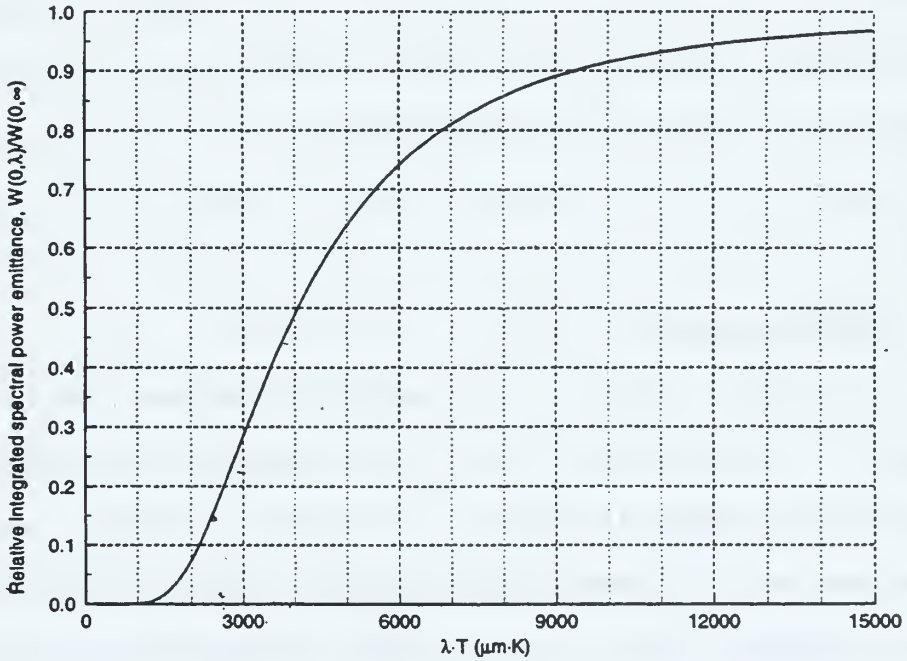

Figure 2.3 W(0,λ) Relative to Total Emittance. (Ref [2])

D. RADIATION FROM OBJECTS

In order to calculate the radiation emitted from a source, we model the source as either a uniformly radiating spherical source(e.g, the sun or a light bulb) or as a planar source(e.g, the exhaust port of a jet engine).

1. Uniform Spherical Source

For a spherical source with a known temperature(in K), an emitting area A, and an emissivity(usually assumed to be less than one;i.e., a graybody object [2]), we can calculate the radiant emittance of the source as

$$W = \varepsilon\sigma T^4 \qquad (II-7)$$

Then we can find the total power from the source as

$$P = W \cdot A \qquad (II-8)$$

and the radiant intensity by realizing that it is emitting uniformly into a sphere of 4π steradians:

$$J = \frac{P}{4\pi} \qquad (II-9)$$

2. Planar Source

For a planar source, we cannot assume that the radiation is symmetrical so the power is radiated nonuniformly from such a source. A standard procedure is to model the source as a *Lambertian emitter*, where both power and radiant intensity will vary with the observation angle. For such a source it can be shown that the radiance is [2]

$$N = \frac{W}{\pi} = \frac{\varepsilon\sigma T^4}{\pi} \qquad (II-10)$$

E. TRANSMISSION OF IR THROUGH THE EARTH'S ATMOSPHERE

Most infrared systems must view their targets through the earth's atmosphere. Before it reaches the infrared sensor, the radiant flux from the target is selectively absorbed by several of the atmospheric gases, and scattered away from the line of sight by small particles suspended in the atmosphere.

When the particles are small compared with the wavelength of the radiation, the process is known as Rayleigh scattering and exhibits a λ^{-4} dependence. For larger particles, the scattering is independent of wavelength. Scattering by gas molecules in the atmosphere is, therefore, negligibly small for wavelengths longer than 2 um. Smoke and light mist particles are also usually small with respect to infrared wavelengths, and infrared radiation can, therefore, penetrate further through smoke and mists than visible radiation. However, rain, fog particles, and aerosols are larger and, consequently, scatter infrared and visible radiation to a similar degree.

In the infrared portion of the spectrum, the absorption process poses a far more serious problem than does the scattering process. The spectral transmittance measured over a 6000 ft horizontal path at sea level is shown in Figure 2.4. The molecule responsible for each absorption band, either water vapor, carbon dioxide, or ozone, is shown in

the lower part of the figure. Inspection of Figure 2.4 reveals the presence of atmospheric windows, i.e, regions of reduced atmospheric attenuation.

IR detection systems are designed to operate in these windows. Combinations of detectors and spectral bandpass filters are selected to define the operating region to conform a window to maximize performance and minimize background contributions.

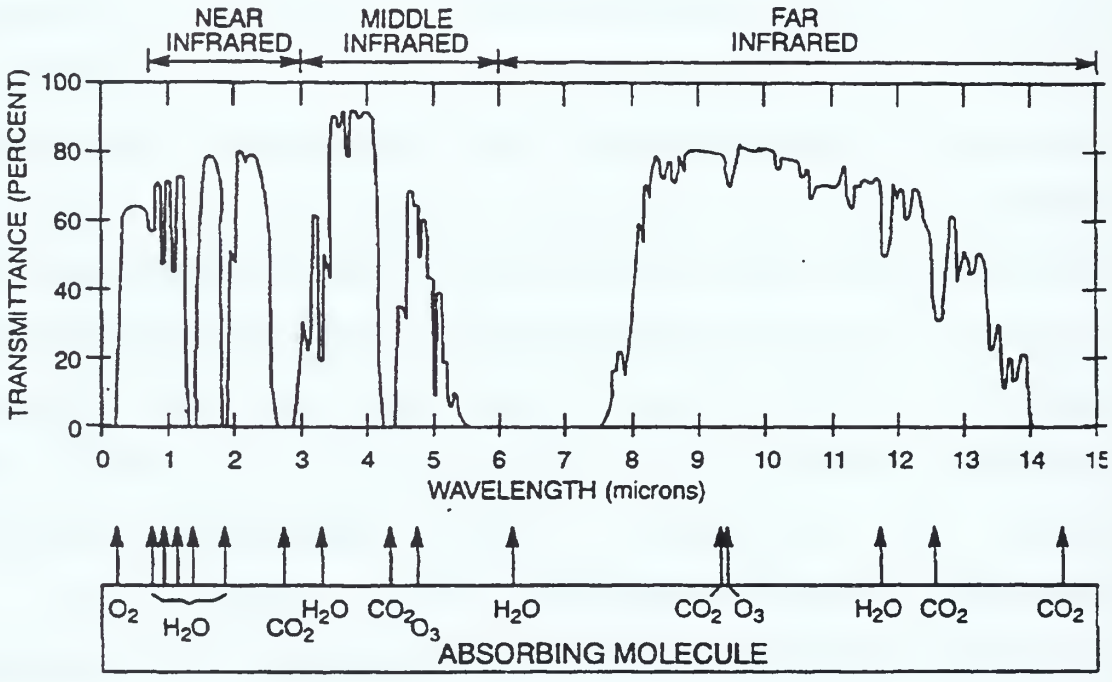

Figure 2.4 Transmittance of Atmosphere over one Nautical Mile (NM) Sea Level Path (Infrared Region). (From Ref [3])

F. IR DETECTORS

The detector is the heart of every IR system because it converts scene radiation into some other measurable form; this can be an electrical current, or a change in some physical property of the detector.

In general, an infrared detector in a particular set of operating conditions is characterized by two performance measures: the responsivity R and the specific detectivity D*. The responsivity is the gain of the detector expressed in volts of output signal per watt of input signal. The specific detectivity is the detector output signal-to-noise ratio for one watt of input signal, normalized to a unit sensitive detector area and a unit electrical bandwidth. The different types of IR detectors may be divided into two broad classes, namely thermal detectors and photon, or quantum, detectors.

1. Thermal Detectors

Because thermal detectors have been used since Herschel's discovery of the infrared portion of the spectrum, it is appropriate to consider them first. They are distinguished as a class by the observation that the heating effect of the incident radiation causes a change in some physical property of the detector.

Since most thermal detectors do not require cooling, they have found almost universal acceptance in certain field

applications in which it is impractical to provide such cooling. Because (theoretically) they respond equally to all wavelengths, thermal detectors are often used in radiometers. The time constant of a thermal detector is usually a few milliseconds or longer, so that they are rarely used in search systems or in any other application in which high data rates are required.

2. Photon Detectors

Most photon detectors have a detectivity that is one or two orders of magnitude greater than that of thermal detectors. This higher detectivity does not come for free, however, since many photon detectors will not function unless they are cooled to cryogenic temperatures. Because of the direct interaction between the incident photons and the electrons of the detector material, the response time of photon detectors is very short; most have time constants of a few microseconds rather than the few milliseconds typical of thermal detectors.

Finally, the spectral response of photon detectors, unlike that of thermal detectors, varies with wavelength. Curves of D* versus wavelength are shown in Figure 2.5 for different types of photon detectors.

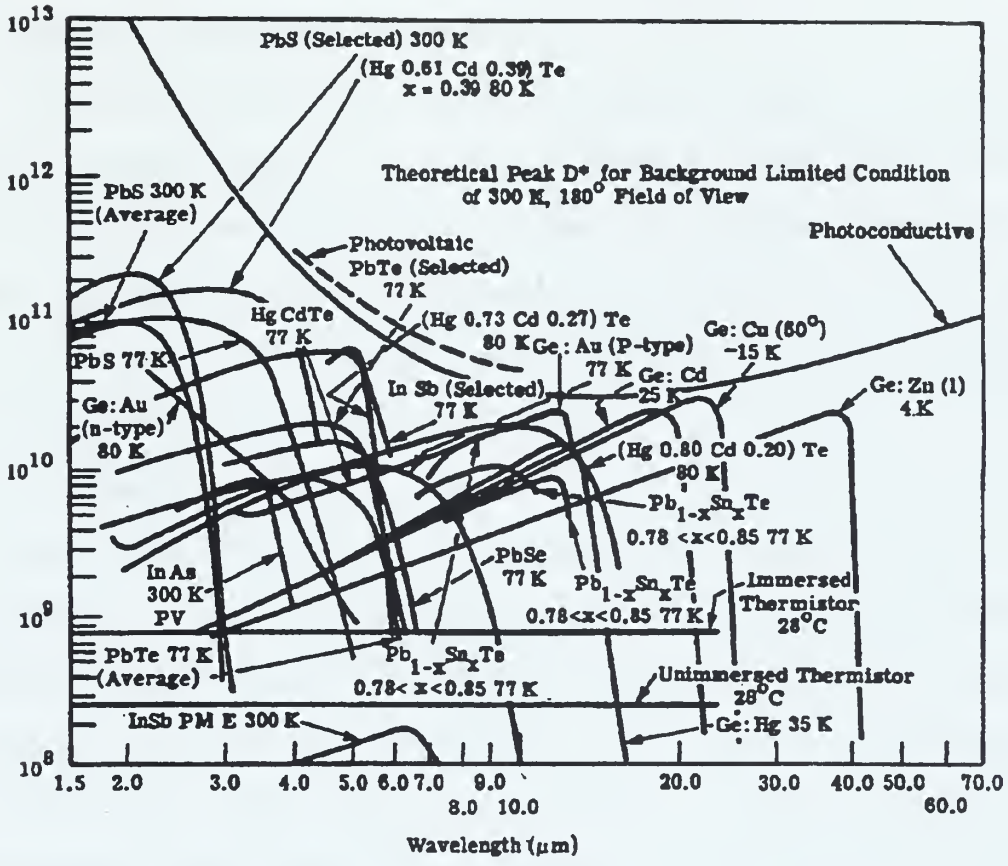

Figure 2.5 D* vs. λ for Representative Detectors (From Ref [2])

III. PYROPHORIC MODEL

A. GENERAL DESIGN REQUIREMENTS

Infrared decoys are used in modern times to protect combat systems from IR tracking threats. The most common examples of IR decoys are IR flares. IR decoys are used to protect aircraft from heat-seeking missiles. Some key requirements for the design specifications of an expendable decoy are discussed in the following.

1. Peak Intensity

Peak intensity is normally the most important requirement. IR decoys must radiate with sufficient intensity and at least exceed the intended target's radiant intensity in the band of interest. This can be accomplished by controlling the decoy temperature or by the use of selective emitters that have a higher emissivity in the band of interest. A common design problem is illustrated in the spectral intensity versus wavelength plot of Figure 3.1. The relative spectral distribution between a decoy (a small hot source) and an aircraft target (a large, relatively cool source) is shown. From the viewpoint of the decoy designer, it is advantageous if a significantly higher percentage of the optical signal at the detector, within the ' decoy band' is due to the decoy rather than the target. Finally, the peak intensity is the primary driver for the decoy weight,

volume, and cost that must be smaller, lighter, and cheaper,respectively, than the protected target.

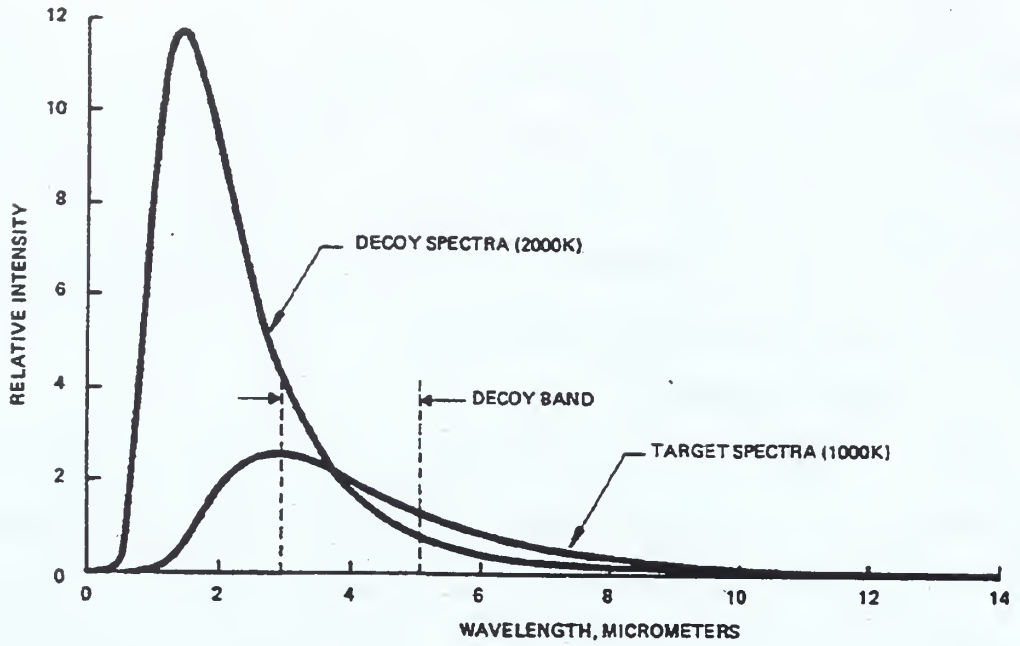

Figure 3.1 Typical Decoy and Target Spectra (From Ref [4])

2. Flare Intensity Rise Time

A decoy must persist long enough to ensure that no possibility of target reacquisition remains. Consequently, it must maintain a credible signature until the original target is no longer in the threat field-of-view. If this is not the case, it is necessary to deploy a second flare. Additionally, the decoy must achieve an effective intensity quickly enough to capture the seeker before leaving the threat field-of-view. The diameter of the threat field-of-

view at the time of decoy deployment is usually less than 200 m. This means that effective operational intensity levels must be achieved in a fraction of a second [Ref 4]. The exact value of the time to rise to peak radiant intensity depends of the chemical composition and packing. Exact values are difficult to find in the open literature.

B. DEVELOPMENT OF THE PYROPHORIC MODEL

The pyrophoric model must simulate changes in both the time and space domains. The modeling procedure for calculating the in-band radiant intensity is summarized in Figure 3.2.

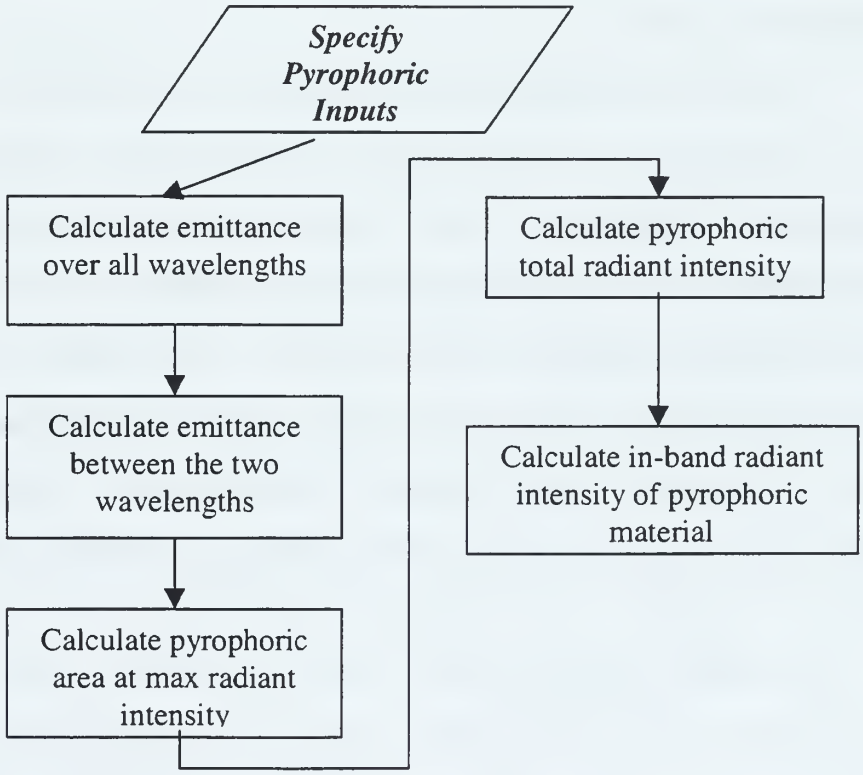

Figure 3.2 Calculation of In-Band Radiant Intensity.

1. Time Domain Variations

The emittance over all wavelengths for any hot object follows Planks radiation equation is given from the *Stefan-Boltzmann* Law

$$W(\lambda,T)_{Pf} = \varepsilon\sigma T_{Pf}{}^{4} \qquad (III-1)$$

where the *Stefan Boltzmann* radiation constant is [Ref 2]

$$\sigma = 5.67\times10^{-12} W\cdot cm^{-2}\cdot{}^{\circ}K^{-4}$$

ε is the emissivity of the pyrophoric and T_{Pf} a specified temperature. The approximation of a graybody model is used to approximate the in-band radiant emittance for these expendables [Ref 4].

The M-file **plankpf.m** recorded for reference in Appendix B is used to calculate for a particular temperature the integrated emittance over a band of wavelengths. The 3-to 5-micron band is very common for a detector because this band has less atmospheric attenuation. The emittance $W(\lambda_1,\lambda_2)_{Pf}$ that lies inside the detector's band is obtained using the M-file program cited above. The fraction of the emitted power that lies between two wavelengths λ_1 and λ_2 is

$$\eta_{Pf} = W(\lambda_1,\lambda_2)_{Pf} \Big/ W(\lambda,T)_{Pf} \qquad (III-2)$$

The pyrophoric source is modeled as a uniformly radiating spherical source with radius r_{MAX} at the instant

for which a maximum occurs in the radiant intensity t_p. The associated area is

$$A_{Pf} = 4\pi \cdot r_{MAX}^2 \qquad (III-3)$$

The peak radiant intensity J_{MAX} of an isotropic radiator is [Ref 2]

$$J_{MAX} = \left(\left(\varepsilon \sigma T_{Pf}^4 \right) \Big/ \left(4\pi \right) \right) \cdot A_{Pf} \qquad (III-4)$$

The total radiant intensity that lies inside the detector's band is

$$J(\lambda_1, \lambda_2)_{Pf} = J_{MAX} \cdot \eta_{Pf} \qquad (III-5)$$

From the input t_p for the pyrophoric burn, the time radiant intensity distribution of the pyrophoric burn can be predicted. Two operational properties are desirable. Ideally, the pyrophoric time function will achieve peak intensity quick enough to capture missile seeker attention before leaving the field-of-view. Furthermore, it should persist long enough to ensure that no possibility of target reacquisition remains. The probability density function (pdf) of the standard Gamma distribution [Ref 5] has sufficient flexibility to model these two basic properties. The flow chart that summarizes the development of the

temporal variation in radiant intensity distribution of the pyrophoric burn is shown in Figure 3.3.

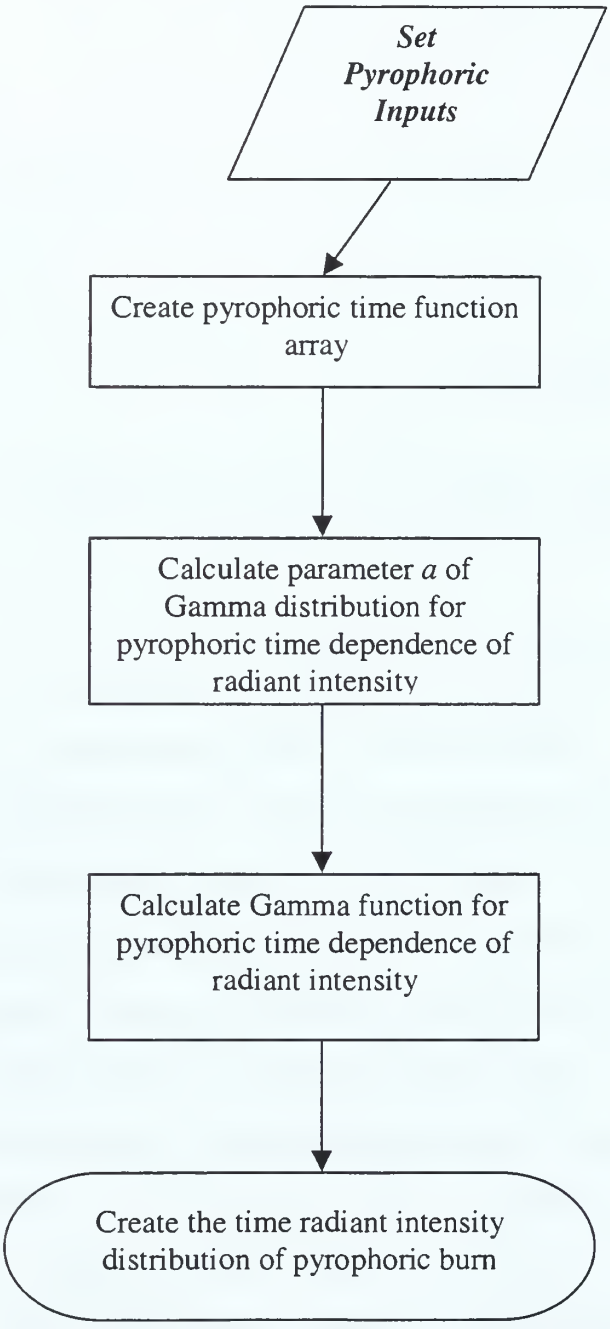

Figure 3.3 The Time Radiant Intensity Distribution Structure of Pyrophoric Burn.

Other inputs such as that corresponding to initial time t_1 and final time t_2 for the simulation to be performed will lead to the development of a time-function-array $\bar{t}$.

The Gamma distribution, which is a continuous random variable (RV), is defined as

$$f(t;a,\beta)=\frac{1}{\beta^a\Gamma(a)}t^{a-1}e^{-t/\beta} \qquad (III-6)$$
$$t\geq 0$$
$$a>0 \quad , \quad \beta>0$$

Because of interest in modeling the temporal variation in radiant intensity, the *t* parameter is used to define time dependence. The standard Gamma distribution [Ref 5] has $\beta=1$ so the pdf of a RV modeled as a standard Gamma RV is

$$f(t;a)=\frac{1}{\Gamma(a)}t^{a-1}e^{-t} \qquad (III-7)$$
$$t\geq 0$$
$$a>0$$

In Appendix C, a short proof is presented that demonstrates that the peak in the distribution satisfies the condition

$$t_p=a-1 \qquad (III-8)$$

From this relation the values for the parameter *a* for different values of the pyrophoric peak times are predicted. Using the M-file **gammaz.m**, recorded for reference in Appendix B, we calculate the Gamma function $\Gamma(\alpha)$ and

employ the main program to predict the temporal variation in the radiant intensity as

$$J(t) = J_{MAX} \cdot f(t,a) \qquad (III-9)$$

A plot of equation (III-9) for the conditions t_p=1sec, T_{pf}=2000K, and r_{MAX}=1.0m for a pyrophoric time array lasting 8s are shown in Figure 3.4.

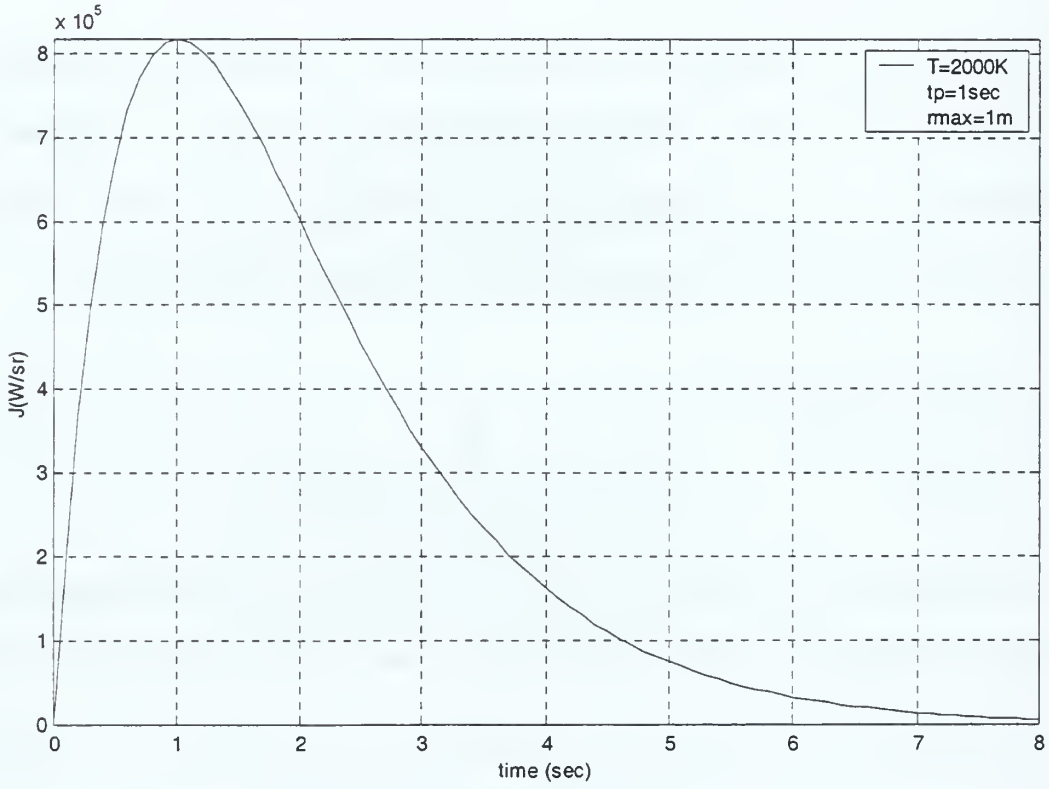

Figure 3.4 The Time Radiant Intensity Distribution of Pyrophoric Burn

2. Space Domain

The flow chart that is followed to develop the radiant intensity distribution of pyrophoric burn in the space domain is shown in Figure 3.5.

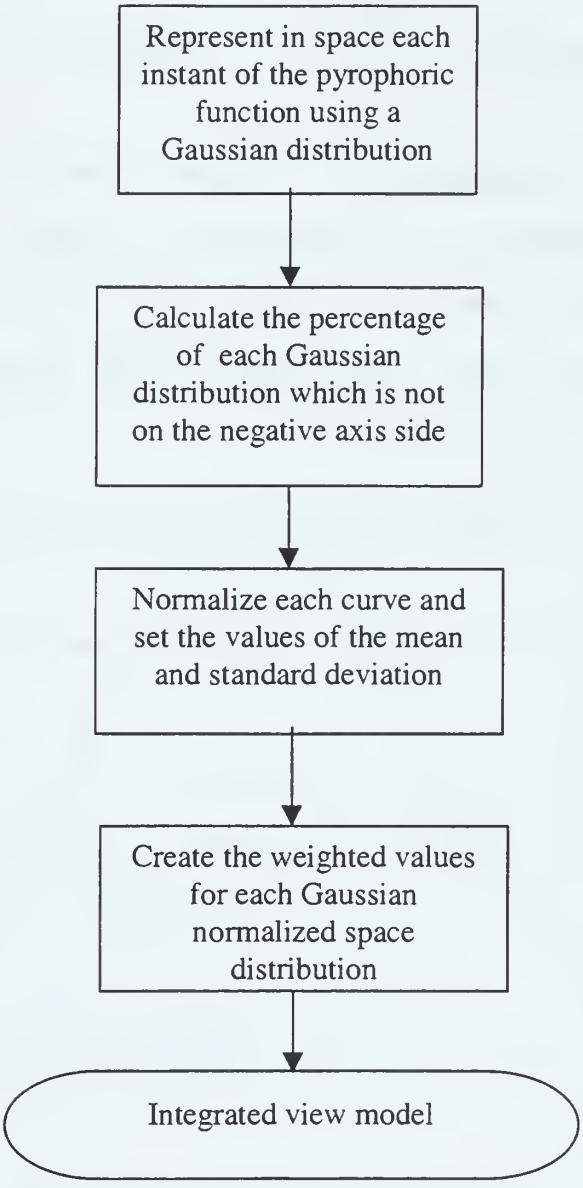

Figure 3.5 Normalized Space Distribution Structure

It is assumed that the spatial distribution for each instant of the pyrophoric burn is a Gaussian distribution. Generally, a continuous random variable X is said to have a Gaussian distribution if the pdf is

$$f(x;\mu,\sigma)=\frac{1}{\sqrt{2\cdot\pi}\cdot\sigma}\cdot e^{-(x-\mu)^2/2\cdot\sigma^2} \qquad -\infty<x<\infty \qquad (III-10)$$

where μ is the mean and σ is the standard deviation. One Gaussian distribution is shown in Figure 3.6. The Gaussian pdf is symmetric about the mean and the standard deviation is the distance from the mean to the point at which the slope of the curve changes.

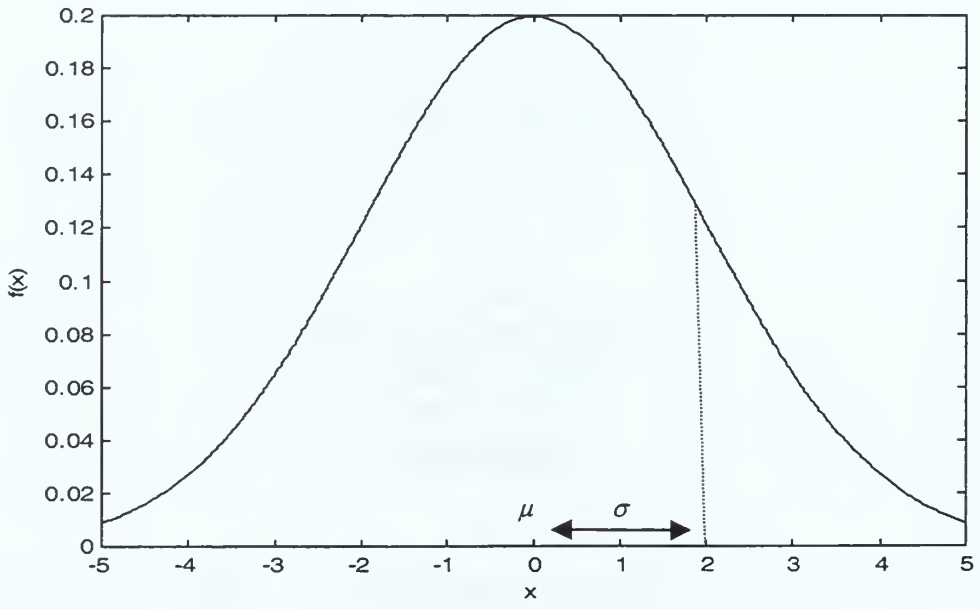

Figure 3.6 Graph of a Gaussian Distribution

In Appendix C a proof is presented that demonstrates that for a Gaussian random variable Z, the area under the curve from zero to infinity is given by equation (C-12), which is reproduced here for convenience:

$$Q(z=-\frac{\mu}{\sigma}) = \frac{1}{2}\cdot erfc\left(-\mu/\sigma\cdot\sqrt{2}\right) \qquad (III-11)$$

From the inputs t_p, r_{MAX}, and the pyrophoric time function array $\bar{t}$, the following parameters can be obtained:

$$u_p = \frac{r_{MAX}}{t_p} \quad (constant\ pyrophoric\ velocity) \qquad (III-12)$$

$$\vec{r}_{MAXt} = u_p \cdot \vec{t} \quad (temporal\ dependent\ pyrophoric\ radius) \qquad (III-13)$$

$$\vec{r}_{NORM} = \frac{\vec{r}_{MAXt}}{r_{MAX}} \quad (normalized\ pyrophoric\ radius) \qquad (III-14)$$

At each instant of the pyrophoric burn, it is assumed that the spatial radiant intensity function is a Gaussian distribution with a mean value

$$\mu = \frac{\vec{r}_{MAXt}}{r_{MAX}} = \frac{u_p \cdot \vec{t}}{u_p \cdot t_p} = \vec{t}/t_p \qquad (III-15)$$

From (III-11), the area under each curve from zero to infinity is

$$Q(\bar{t}) = \tfrac{1}{2} \cdot erfc\left(\frac{-\frac{\bar{t}}{t_p}}{\sigma \cdot \sqrt{2}} \right) \qquad (III-16)$$

which is positive and less than one.

For each element of the array $\bar{t}$, the value of the temporal distribution is given by

$$f(\bar{t}, a) = \frac{1}{\Gamma(a)} \cdot \bar{t}^{\,a-1} \cdot e^{-\bar{t}} \qquad (III-17)$$

Now in equation (III-10) we use x= $\bar{r}_{NORM}$ and μ= $\bar{t}/t_p$ to obtain the normalized space distribution in the pyrophoric burn as

$$f(\bar{r}_{NORM}, \bar{t}/t_p, \sigma) = \frac{1}{\sqrt{2\pi} \cdot \sigma} e^{-\left(\bar{r}_{NORM} - \bar{t}/t_p\right)^2 / 2\sigma^2} \qquad (III-18)$$

The next step is to use 1/Q(t) to normalize the corresponding equation (III-18). The result, which is a pdf defined over positive $\bar{r}_{NORM}$, has an area under the curve equal to one. This result is multiplied by equation (III-9) to obtain

$$j\left(\bar{r}_{NORM}, \bar{t}/t_p\right) = f(\bar{r}_{NORM}, \bar{t}/t_p, \sigma) \times J(\bar{t}) \times \left(1/Q(\bar{t})\right) \qquad (III-19)$$

where the space integration of the space-time distribution satisfies the relation

$$\int j\left(\vec{r}_{NORM}, \vec{t}/t_p\right) dr = J(\vec{t})$$

This forces the resulting space-time distribution *j* to have a space integrated area equal to J(t). One example is shown in Figure 3.7 where successive curves represent time steps of 0.2s.

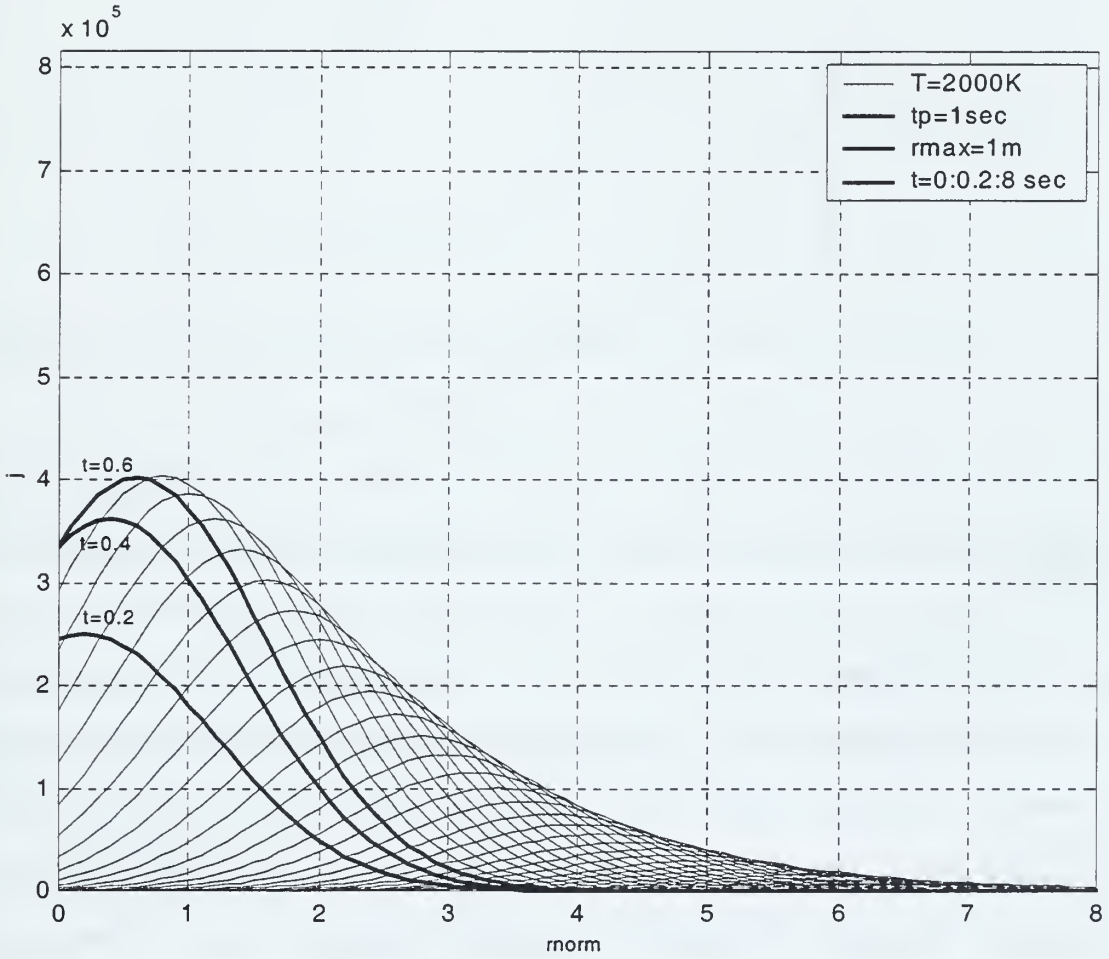

Figure 3.7 Pyrophoric Space Distribution

The last major step, see the flowchart in Figure 3.5, is to create the space domain pyrophoric integrated view-model. The general idea is to pick a curve from Figure 3.7 which corresponds to one instant of time t, as illustrated in Figure 3.8.

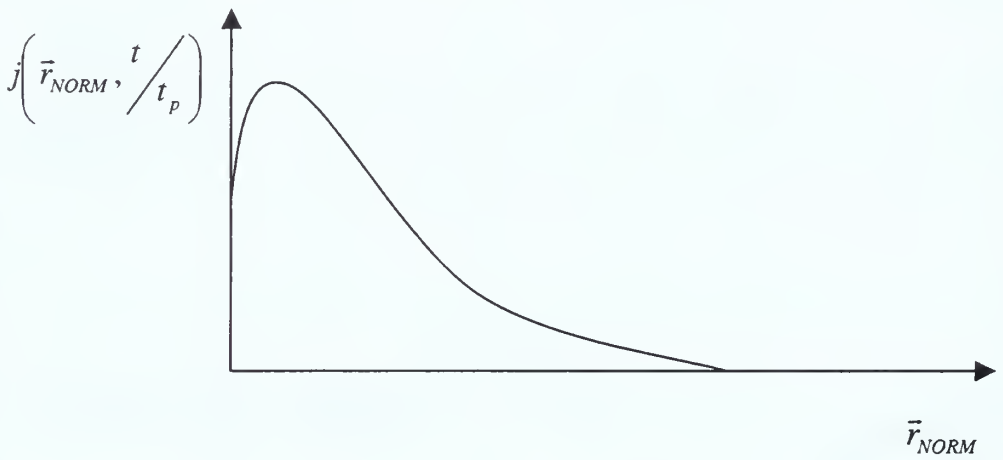

Figure 3.8 Pyrophoric Space distribution for one instant of time t.

As represented on Figure 3.9, the pyrophoric source is modeled as spherical. It is assumed that an external remote observer will 'view' the source and perceive radiation integrated along a thin line x. The total radiant intensity distribution at a specific instant of time will consist of the integration of radiant intensity over each distance $|\bar{r}_i|$, where $|\bar{r}_i|$ is the distance between the center of the

distribution and some point along the line x. The line x is shifted by $|\bar{r}_o|$ from the distribution center.

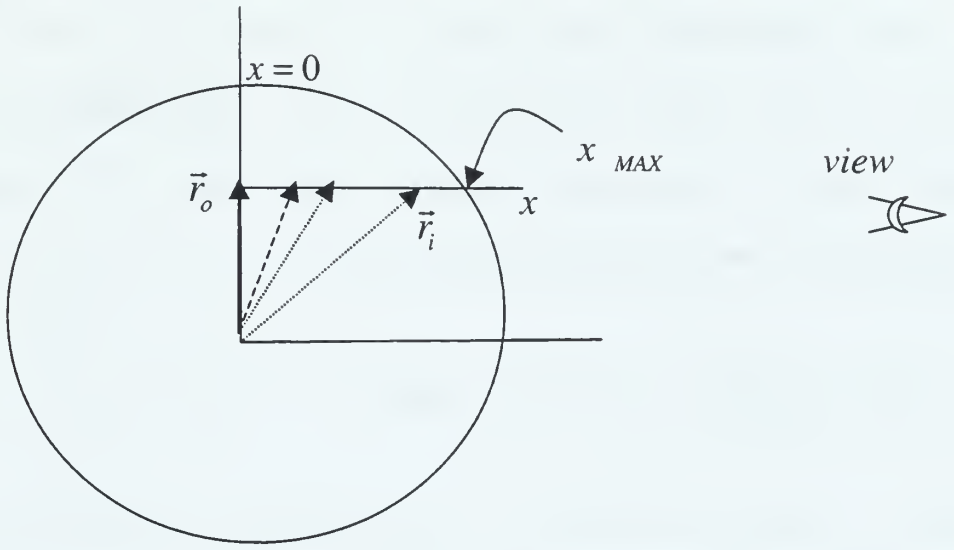

Figure 3.9 The integrated pyrophoric model projection

Analytically, for each distance from the center of the distribution $|\bar{r}_o|$, a fixed number of uniformly spaced points are selected along the line x from x=0 to $x=x_{MAX}$. The distance $|\bar{r}_i|$ that connects each of these points with the center of the distribution is given by

$$|\vec{r}_i| = \sqrt{|\vec{x}_i|^2 + |\vec{r}_o|^2} \qquad (III-20)$$

where $|\bar{x}_i|$ the distance along the line x. In the computer code, an index k is generated as

$$k = \left(\left| \vec{r}_i \right| \Big/ \max\left(\left| \vec{r}_{NORM} \right| \right) \right) \times size\left(\vec{r}_{NORM} \right) \qquad (III-21)$$

so the integrated-view radiant intensity for the specific $|\bar{r}_i|$, i.e, one point is given by $j_t(k)$. The summation of all the radiant intensity values for each $|\bar{r}_i|$ give the integrated-view radiant intensity

$$J_V\left(\vec{r}_o, t\right) = \sum_{x_i}^{x_{MAX}} j_t\left(k\right) \qquad k \quad index \qquad (III-22)$$

which is easily computed. Alternatively, an equivalent but more analytical representation is

$$J_V\left(\vec{r}_o, t\right) = \sum_{x_i}^{x_{MAX}} j_t\left(\vec{r}_i, \frac{t}{t_p} \right) \qquad (III-23)$$

Typical distributions of integrated-view radiant intensities for pyrophoric burns lasting eight seconds are shown in Figure 3.10. The horizontal axis of Figure 3.10 is specified in terms of the index variable of the array $\bar{r}_o$. It is observed that the curve with the maximum area corresponds to the instant $t=t_p$.

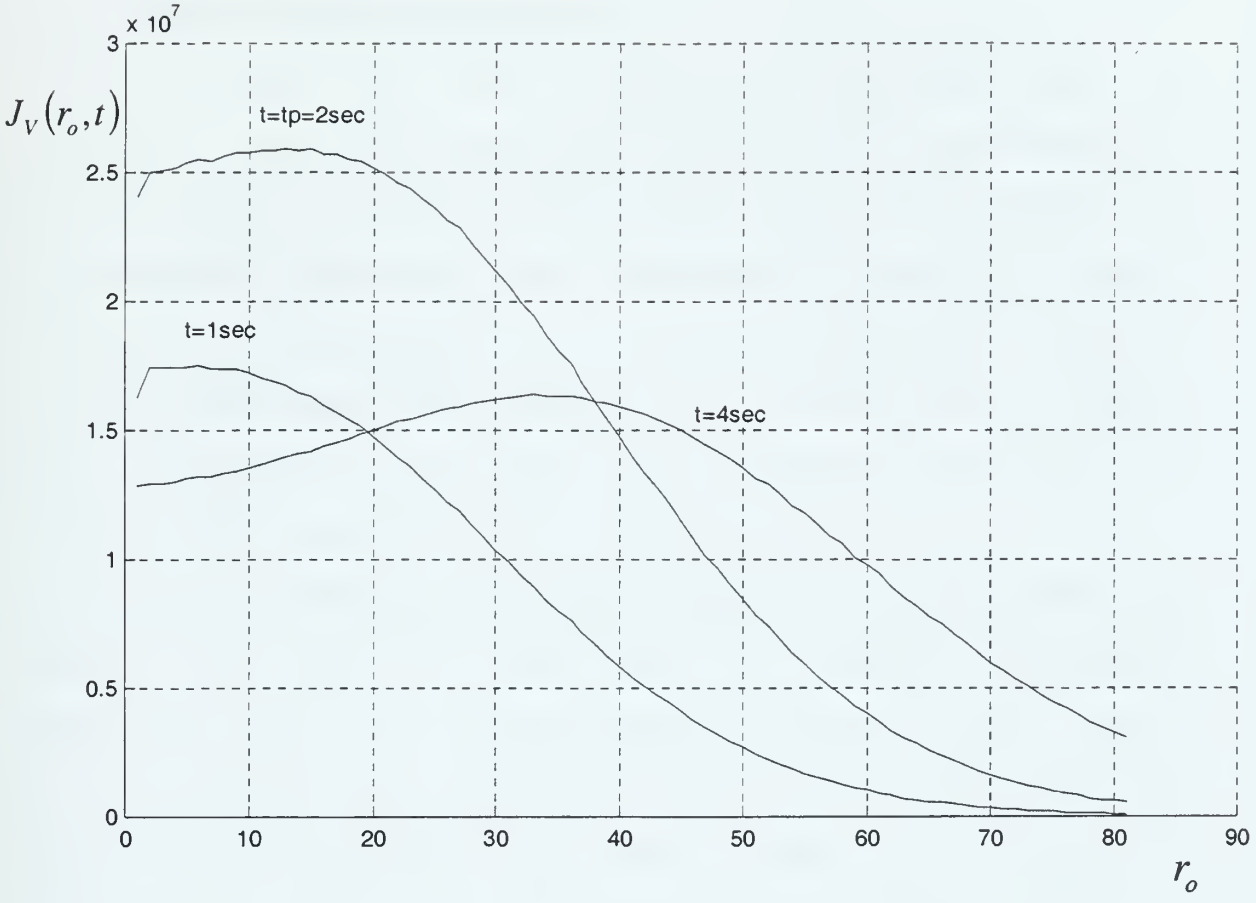

Figure 3.10 Integrated-view Radiant Intensity Distribution Curves for the Pyrophoric Model.

IV. PLUME MODEL

A. GENERAL DESIGN REQUIREMENTS

The plume of the aircraft can dominate the IR signature. This is no doubt due to the considerable radiant energy created from the combustion process. Measurements of the radiation from military a aircraft's plume are highly classified. Fortunately, it is not too difficult to make order-of-magnitude calculations of the radiation by using only temperature and dimensional information that can be found in the open literature [Ref 4].

During afterburning, which results in an increase in thrust, the rate at which fuel is consumed increases drastically and the plume becomes the dominant source. Also, if the aircraft is viewed from the forward hemisphere or from an aspect angle at which the tailpipes are not visible, the plume is the only source of radiation available. The calculation of the exact radiant intensity of the plume is extremely difficult since both temperature and emissivity vary in a complex manner through out its volume.

The exhaust temperature contours for a typical turbojet engine with and without afterburner are shown in Figure 4.1.

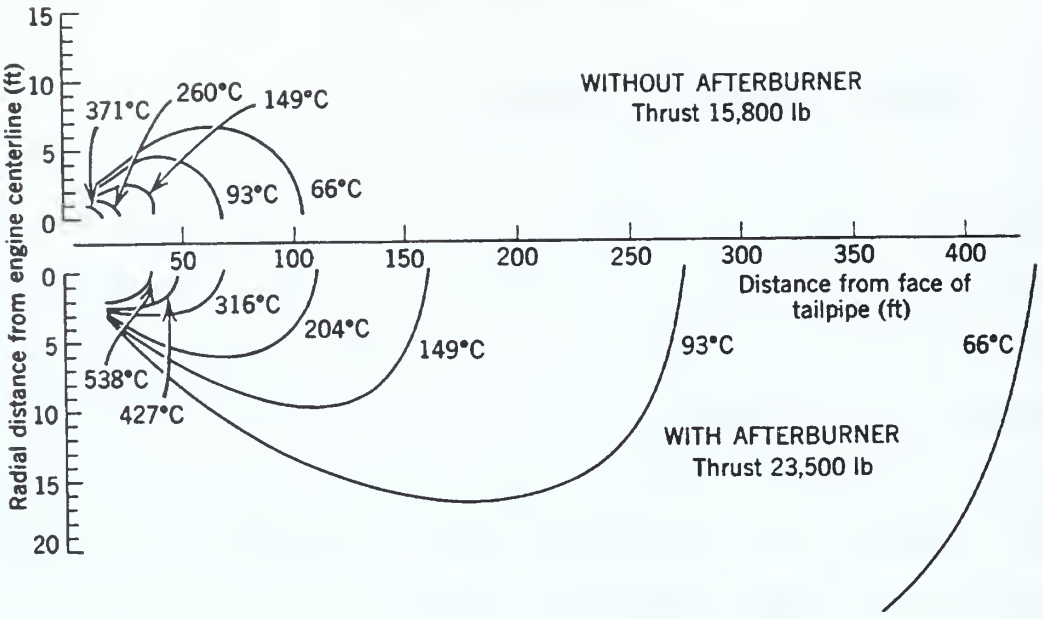

Figure 4.1 Exhaust Temperature Contours for a JT4A Turbojet Engine with and without Afterburner (From Ref [1])

We can see that when afterburner is turned on, the temperature and size of the plume increase appreciably. If we integrate over the entire plume in order to estimate its radiant intensity, the radiant intensity will be several times that of the hot tailpipe. For in-band engineering calculations, a plume can be approximated as a graybody with an emissivity of 0.9 [Ref 1].

The steps that are followed to calculate the radiant intensity of the plume model is shown in Figure 4.2.

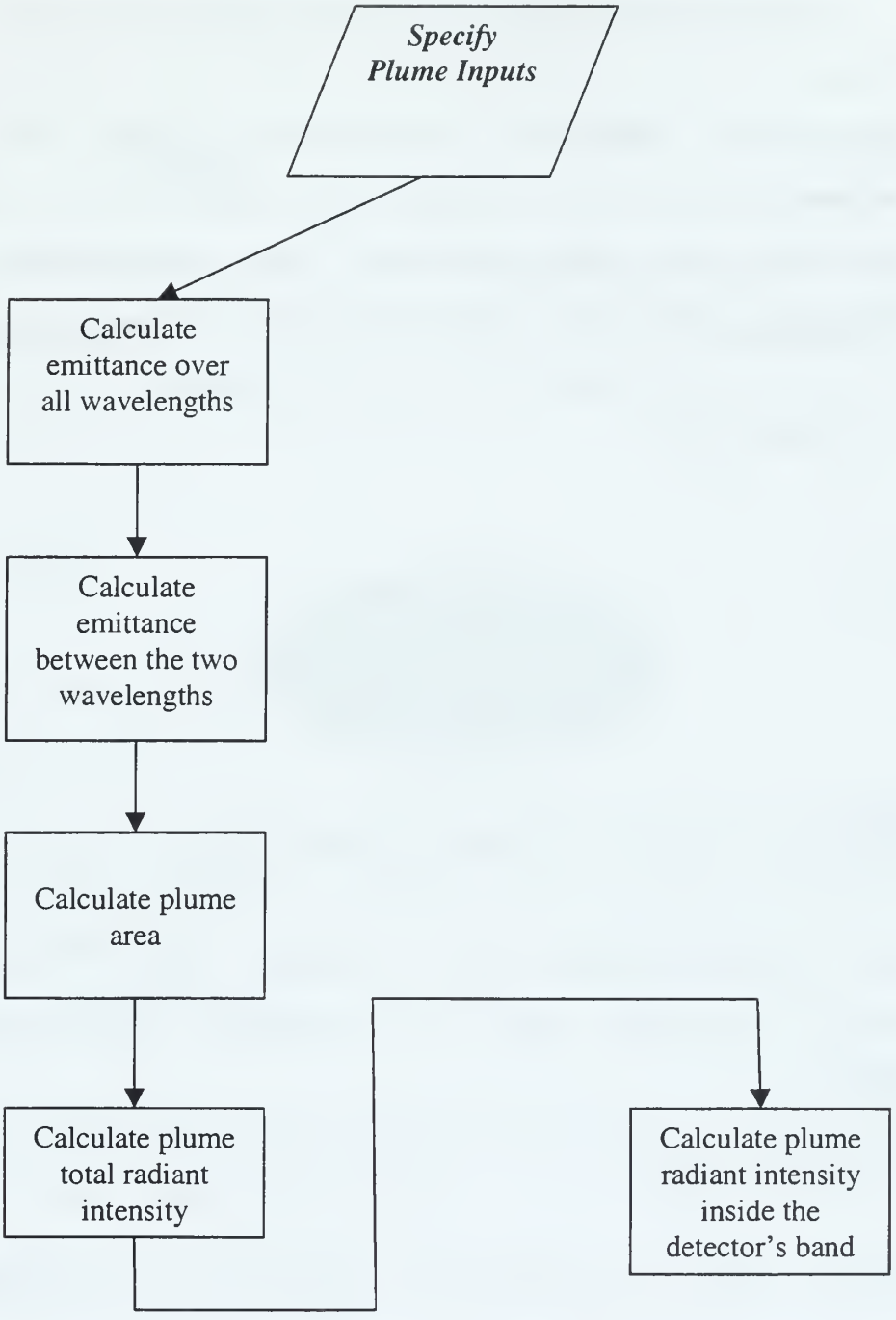

Figure 4.2 Calculation of In-Band Radiant Intensity.

B. DEVELOPMENT OF THE PLUME MODEL

The assumed geometric model for the plume, shown in Figure 4.3, is an ellipse. This is used to model a three-dimensional radiating ellipsoidal source. The required parameters are the included major axis a_{pl}, the minor axis b_{pl}, and the temperature T_{pl} that is assumed constant throughout the plume. The area of the ellipse is

$$A_{pl} = \pi \cdot a_{pl} \cdot b_{pl} \qquad (IV-1)$$

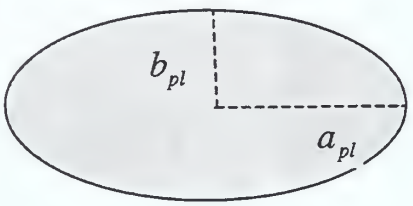

Figure 4.3 Plume's Radiating Source Area.

The *Stefan-Boltzmann* Law is again used to predict the radiant emittance. Here it is applied to the case of the plume:

$$W(\lambda,T)_{Pl} = \varepsilon\sigma T_{Pl}^{\ 4} \qquad (IV-2)$$

where ε here is the effective emissivity of the plume.

Using the M-file **plankpl.m** for the particular temperature with the specific wavelengths of the detector's band, we can compute the total emittance $W(\lambda_1,\lambda_2)$ that lies

inside the detector's band. Next, we find the fraction of the emittance that lies between wavelengths λ_1 and λ_2 as

$$\eta_{Pl} = W(\lambda_1, \lambda_2)_{Pl} \Big/ W(\lambda, T)_{Pl} \qquad (IV-3)$$

The physical model for the plume source is assumed to behave as a *Lambertian emitter* [Ref 2]. Following the standard rule for calculating radiance from total emittance [Ref 2], we get

$$N_{Pl} = \frac{\varepsilon\sigma \cdot T_{Pl}^4}{\pi} \qquad (IV-4)$$

The total radiant intensity is then given by

$$J_{Pl} = N_{Pl} \cdot A_{Pl} \qquad (IV-5)$$

and the plume radiant intensity that lies inside the detector's band is

$$J(\lambda_1, \lambda_2)_{Pl} = J_{Pl} \cdot \eta_{Pl} \qquad (IV-6)$$

For later reference, the composite image signal associated with the plume target is defined

$$S = J(\lambda_1, \lambda_2)_{Pl} \qquad (IV-7)$$

V. INTEGRATION OF PYROPHORIC/PLUME MODELS

The main program, recorded in Appendix B, consists of two parts. The general structure of the main program is represented in Figure 5.1.

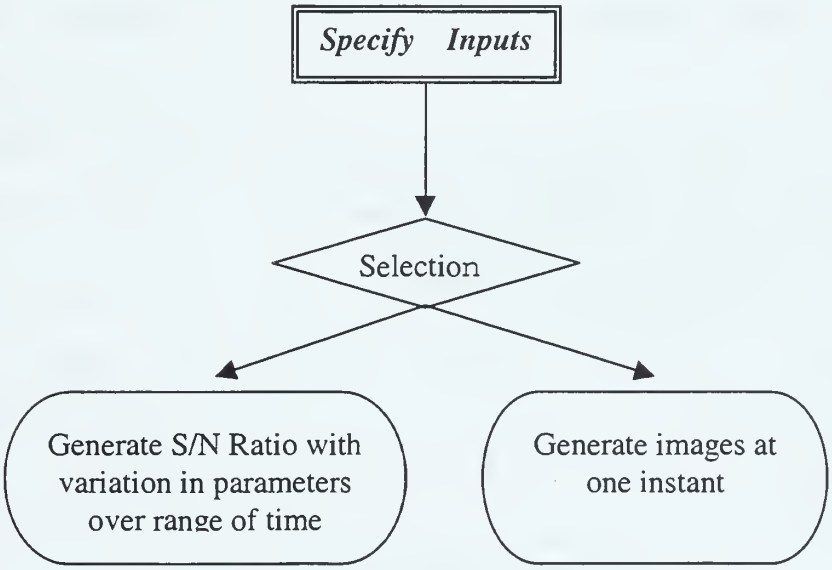

Figure 5.1 General structure of the main program.

Once the inputs have been specified, a selection in the main program permits execution of either the first part, which is the generation of the signal-to-noise ratio (S/N), or the second part, which refers to the generation of the pyrophoric flare and plume images.

The main steps of the procedure which are followed to create S/N are shown in Figure 5.2.

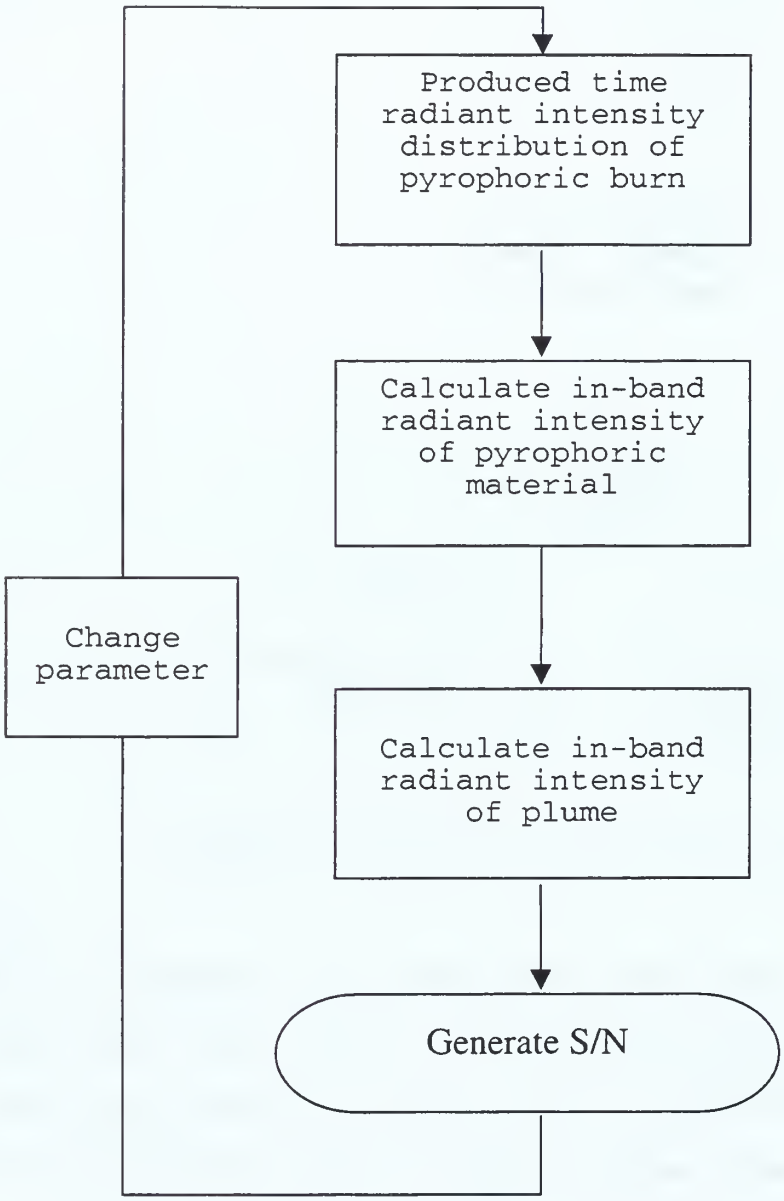

Figure 5.2 S/N Structure.

A. CALCULATION OF S/N

The first step of the flowchart in Figure 5.2, the computation of the time radiant intensity distribution of the pyrophoric burn, was covered in Chapter III. One typical distribution is represented in Figure 3.4.

In the second step of the flowchart, the in-band radiant intensity calculation of the pyrophoric material for each instant of time t is performed. This is found by performing a multiplication of the temporal variation in the radiant intensity J(t), given by the equation (III-9), with the fraction of the emitted power η_{Pf} that lies inside the detector's band (λ_1, λ_2), given by equation (III-2).

Next, the in-band radiant intensity of the pyrophoric material for each instant of time t is obtained from

$$J(\lambda_1, \lambda_2)_{Pf} = J(t) \cdot \eta_{Pfl} \qquad (V-1)$$

and

$$N = J(\lambda_1, \lambda_2)_{Pf} \qquad (V-2)$$

where N is interpreted as a composite noise interference for the missile tracking system.

The in-band radiant intensity calculation of the plume, as given by equation (IV-7) in Chapter IV, is the last component needed in the S/N prediction.

For the calculation of S/N, a situation similar to that shown in Figure 5.3 is assumed, where the plume represents the signal and the pyrophoric the noise.

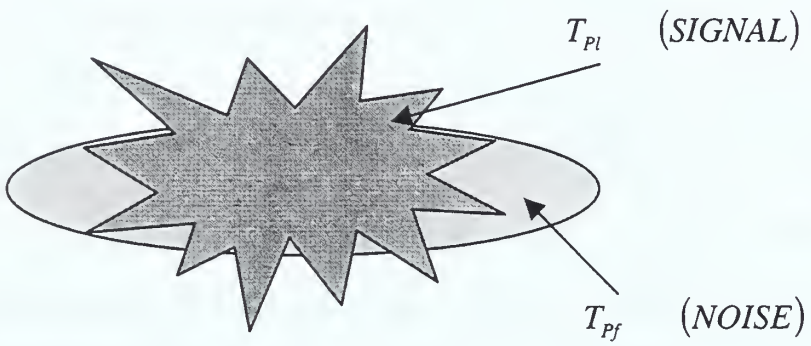

Figure 5.3 S/N Representation.

Based on the preceding discussion, by taking the ratio of the result of equation (IV-7), which represents the composite plume image signal, with the result of equation (V-2), which represents the composite pyrophoric image signal, we obtain an estimate for S/N:

$$\frac{S}{N} = \frac{J(\lambda_1, \lambda_2)_{Pl}}{J(\lambda_1, \lambda_2)_{Pf}} \qquad (V-3)$$

After the estimation of S/N, the main program permits a change in parameters such as pyrophoric temperature T_{Pf}, plume temperature T_{P1}, detector's band wavelengths (λ_1,λ_2), pyrophoric peak time t_p, or radius r_{MAX}, and a recalculation with the new inputs produces a new value for S/N.

The second part in the main program refers to the generation of the pyrophoric and plume images. The main steps of the procedure which are required to create the images are shown in Figure 5.4.

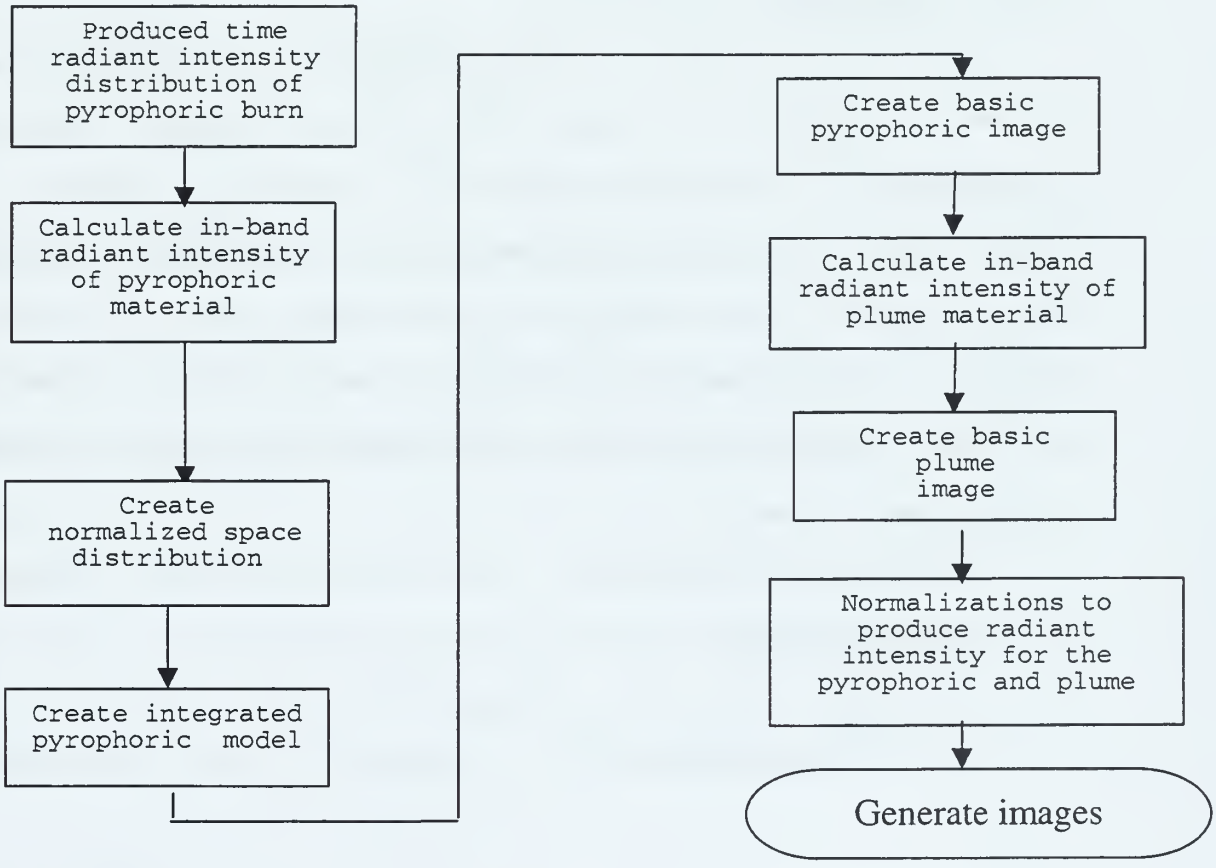

Figure 5.4 Generate Images Structure.

B. GENERATION OF IMAGES

1. Pyrophoric Image Construction

The first four steps of the flowchart in Figure 5.4 have been already created. Specifically, this includes the in-band radiant intensity calculation for each instant of time t. This calculation is done in the first part of the main program which also deals with the S/N generation. Also covered in these four steps is the conversion from the normalized space distribution to the integrated pyrophoric model discussed in Chapter III.

To construct the pyrophoric image, it is assumed that a situation similar to Figure 5.5 is applicable, where FOV represents the field-of-view of the incoming missile, R is the distance at which the missile will detect the pyrophoric source, and N'_{pix} the number of pixels that have to be used in order to visualize the pyrophoric image. These quantities are some of the inputs which are specified at the beginning of the main program.

From this assumption, the missile's window dimension R_{Field} is calculated as

$$R_{Field} = FOV(rad) \times R(m) \quad [m] \qquad (V-4)$$

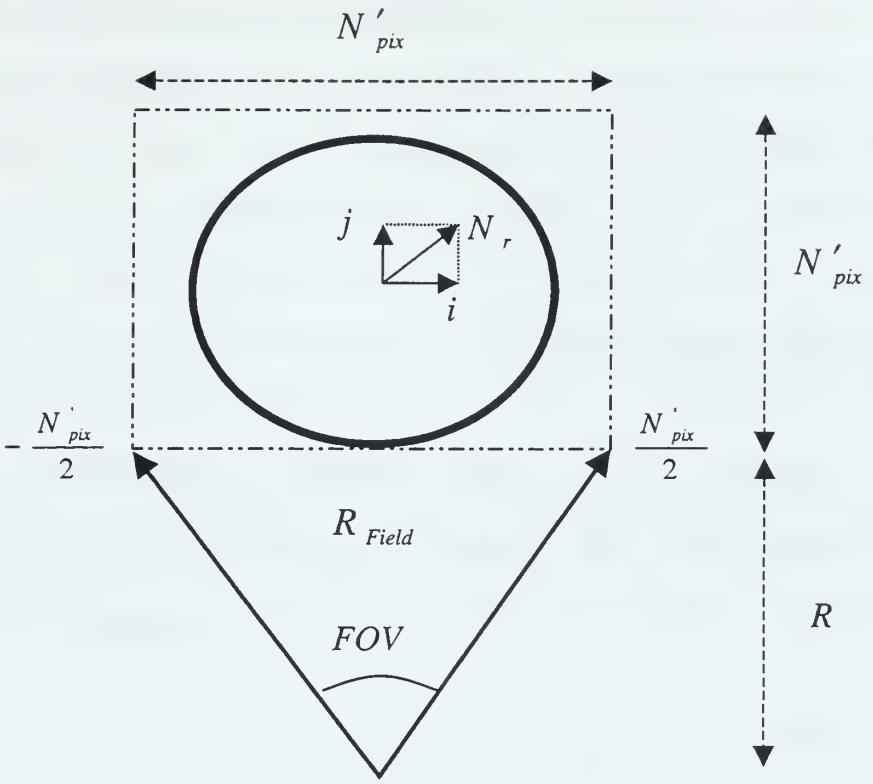

Figure 5.5 Pyrophoric Image Construction.

To specify the distance of the pixels from the center of the pyrophoric image, the pythagorean relation is used

$$N_r = \sqrt{i^2 + j^2} \qquad (V-5)$$

where the i, j indices take values from $-(N'_{pix}/2)$ to $(N'_{pix}/2)$. Once N_r has been calculated for all pixels, the corresponding radial distances are predicted from

$$R_{Pf} = \frac{R_{Field}}{N'_{pix}} \times N_r \qquad (V-6)$$

Next, in the algorithm an index is generated in order to assign a value from the integrated-view radiant intensity, equation (III-23), to each pixel. This index is determined by

$$\ell = \frac{R_{Pf}}{\left(r_{MAX} \cdot \max\left(r_{NORM}\right)\right)} \times size\left(r_{NORM}\right) \qquad (V-7)$$

For each value of this index that corresponds to the inside of the integrated-view radiant intensity array index, the corresponding radiant intensity value is assigned

$$C_{ij} = J_V\left(\ell\right) \qquad (V-8)$$

otherwise the zero value is given to the pixel. Finally, a normalization is performed. The value of each pixel is divided by the summation of all the pixels and multiplied with the in-band pyrophoric radiant intensity, equation(V-1), $(\lambda_1,\lambda_2)_{Pf}$. The normalization rule is therefore equivalent to

$$C_{ij}^{'} = \frac{C_{ij}}{\sum C_{ij}} \times J\left(\lambda_1,\lambda_2\right)_{Pf} \qquad (V-9)$$

where the time dependence is implicit.

2. Plume image construction

From the flowchart in Figure 5.4, the only necessary information to create the basic plume image is the calculation of in-band radiant intensity of plume material, which has been already estimated. Specifically, the in-band radiant intensity calculation for each instant of time t is given from equation (IV-7).

To construct the plume image, it is assumed that the geometric conditions represented by Figure 5.6 are applicable.

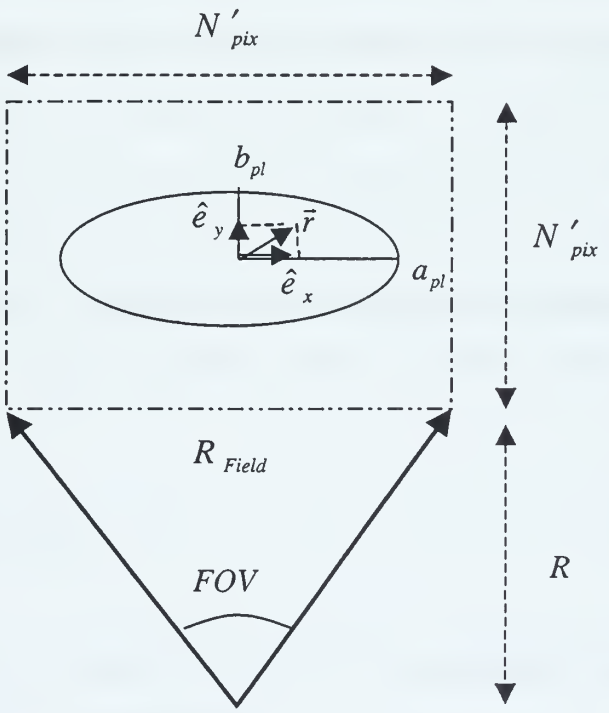

Figure 5.6 Plume Image Construction.

Note the main difference between Figure 5.5 and Figure 5.6 is that the plume is represented here as an ellipse instead of as a circle. The FOV, R, and N'_{pix} are the same quantities that already have been specified for the pyrophoric image construction.

To specify the location of the pixels in the plume image, one vector $\bar{r}$ is created

$$\vec{r} = i\Delta \cdot \hat{e}_x + j\Delta \cdot \hat{e}_y \qquad (V-10)$$

where

- i,j denote indices that take values from $-(N'_{pix}/2)$ to $(N'_{pix}/2)$ with a specific step
- e_x, e_y denote unit vectors along the major axis a_{pl} and minor axis b_{pl}

- $\Delta = \frac{R_{Field}}{N'_{pix}}$ $\qquad (V-11)$

In order to create an ellipsoidal shape, a value has to be assigned to the pixels that belong inside the ellipse's boundary

$$\frac{x^2}{a_{pl}^2} + \frac{y^2}{b_{pl}^2} < 1 \qquad (V-12)$$

where x,y are defined as

- $x = \vec{r} \bullet \hat{e}_x = i\Delta$
- $y = \vec{r} \bullet \hat{e}_y = j\Delta$ $\qquad (V-13)$

Taking the preceding into account and making use of equations (V-11), (V-12), (V-13), we get

$$\frac{i^2}{\left(\frac{a_{pl}}{R_{Field}}\right)^2}+\frac{j^2}{\left(\frac{b_{pl}}{R_{Field}}\right)^2}\le N_{pix}^{'} \qquad (V-14)$$

which provides a convenient rule for defining the interior part of the plume in the computer model.

The numeric values which are assigned to the pixels that define the in-band plume radiant intensity $J(\lambda_1,\lambda_2)_{Pl}$ are taken from plume model and equation (IV-6). After the generation of the ellipsoidal shape, a normalization takes place. The value of each pixel is divided with the summation of all the pixels and multiplied with the in-band plume radiant intensity $J(\lambda_1,\lambda_2)_{Pl}$. This normalization rule is equivalent to

$$C_{ij}^{'}=\frac{C_{ij}}{\sum C_{ij}}\times J(\lambda_1,\lambda_2)_{Pl} \qquad (V-15)$$

The similarity of equation (V-15) to equation (V-9) for the pyrophoric image is apparent.

VI. PRESENTATION OF S/N CURVES

As mentioned in Chapter V, the first part of the main program, which is recorded in the Appendix B, is primarily concerned with the generation of S/N. Once the inputs have been specified, the value of S/N can be extracted for each instant of time. A temporal variation in S/N during the pyrophoric burn time can then be obtained. Next, by changing parameters such as pyrophoric temperature T_{pf}, detector band (λ_1,λ_2), pyrophoric peak time t_p, or radius r_{MAX}, the program computes S/N curves for the new inputs.

A selection of these curves which have been generated through the procedure described are presented in this chapter. A graph that presents an overall variation of S/N during the pyrophoric burn time and a chart that records the minimum S/N for different parameters are included in each figure.

Specifically, Figure 6.1 is a plot of S/N as a function of the pyrophoric function time for different values of pyrophoric temperature T_{pf}. Results were generated for T_{pi}=1000K, t_p=1sec, and r_{MAX}=2m. As expected, an increase in pyrophoric temperature T_{pf} results in a decrease in S/N during the burn period of the pyrophoric material. This is an expected result because it is known from the Stefan-

Boltzmann Law that the emittance increases as the fourth power of the temperature.

Figure 6.2 is a plot of S/N as a function of the pyrophoric function time for different values of radius r_{MAX} corresponding to the instant t_p for which a maximum occurs in the radiant intensity. Results were generated for T_{pf}=2000K, T_{pl}=1000K, and t_p=1sec. We observe that increasing the radius r_{MAX} significantly decreases S/N between the initial and final time of the pyrophoric function. This leads to the conclusion that the radiant intensity output of the pyrophoric flare increases with r_{MAX}.

Figure 6.3 is a plot of S/N as a function of the pyrophoric burn time for different detector bands. Results were generated for T_{pf}=2000K, T_{pl}=1000K, t_p=0.8sec, and r_{MAX}=2m. The curve with the lowest values corresponds to the 1-2 micron band. This band exhibits a large amount of atmospheric attenuation and is not a practical window of detection for a missile. The next band is the 3-5 micron band, which has less atmospheric attenuation. This band, along with the 8-12 micron band, exhibits the lowest amount of atmospheric attenuation and are practical windows of detection for a missile. Making a comparison between these two bands, we see from Figure 6.3 that the curve with the lowest values corresponds to the 3-5 micron band. The next lowest band is the 7-9 micron band. Its curve has lower

values of S/N compared with the 8-12 micron band, but again this band exhibits a large amount of atmospheric attenuation and is not a practical window of detection for a missile.

Figure 6.4 is a plot of S/N as a function of the pyrophoric function time for different values of t_p. Results were generated for T_{pf}=2000K, T_{pl}=1000K, and r_{MAX}=2m. For this case, the minimum S/N corresponding to each t_p are the same. The focus here is the length of time for which the pyrophoric flare will achieve intensity that can capture the missile's seeker. From this plot, we conclude that the flare achieving a peak radiant intensity at a later point in time will have an extended windows of effectiveness. This point is demonstrated in Figure 6.4 by comparing the length of time S/N is below 0.5. The pyrophoric flare reaching its peak at 1.4 seconds has a window of effectiveness of 3.7 seconds, while the flare with t_p=0.8 is only effective for 2.9 seconds. The former is "better" by approximately 25%.

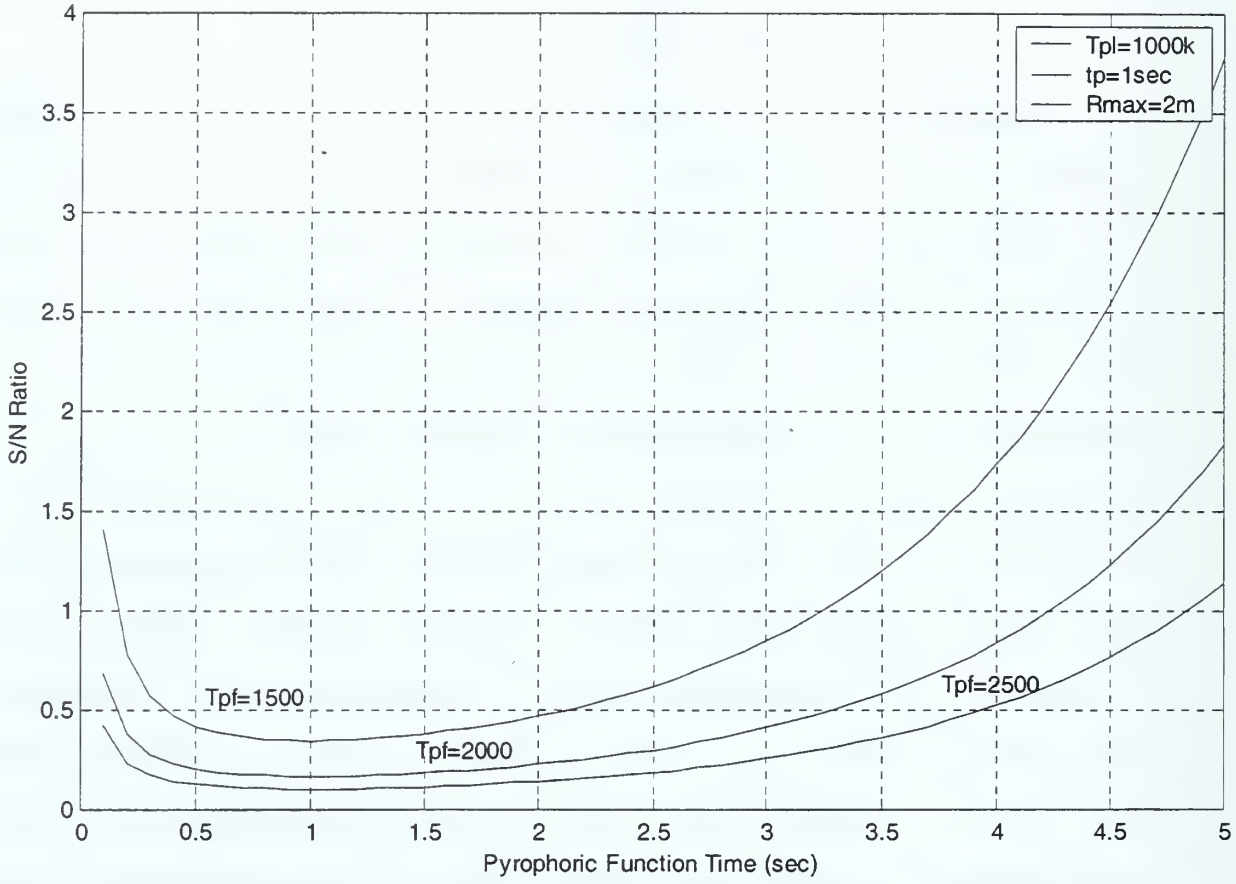

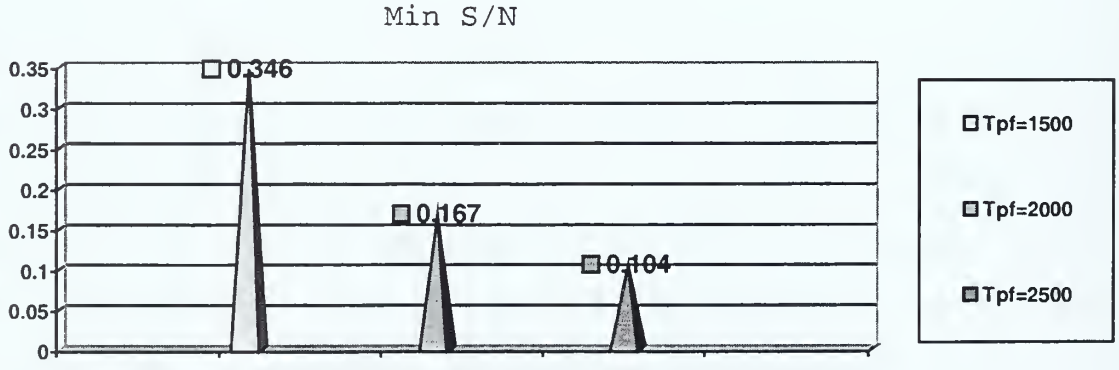

Figure 6.1 S/N for various T_{pf}

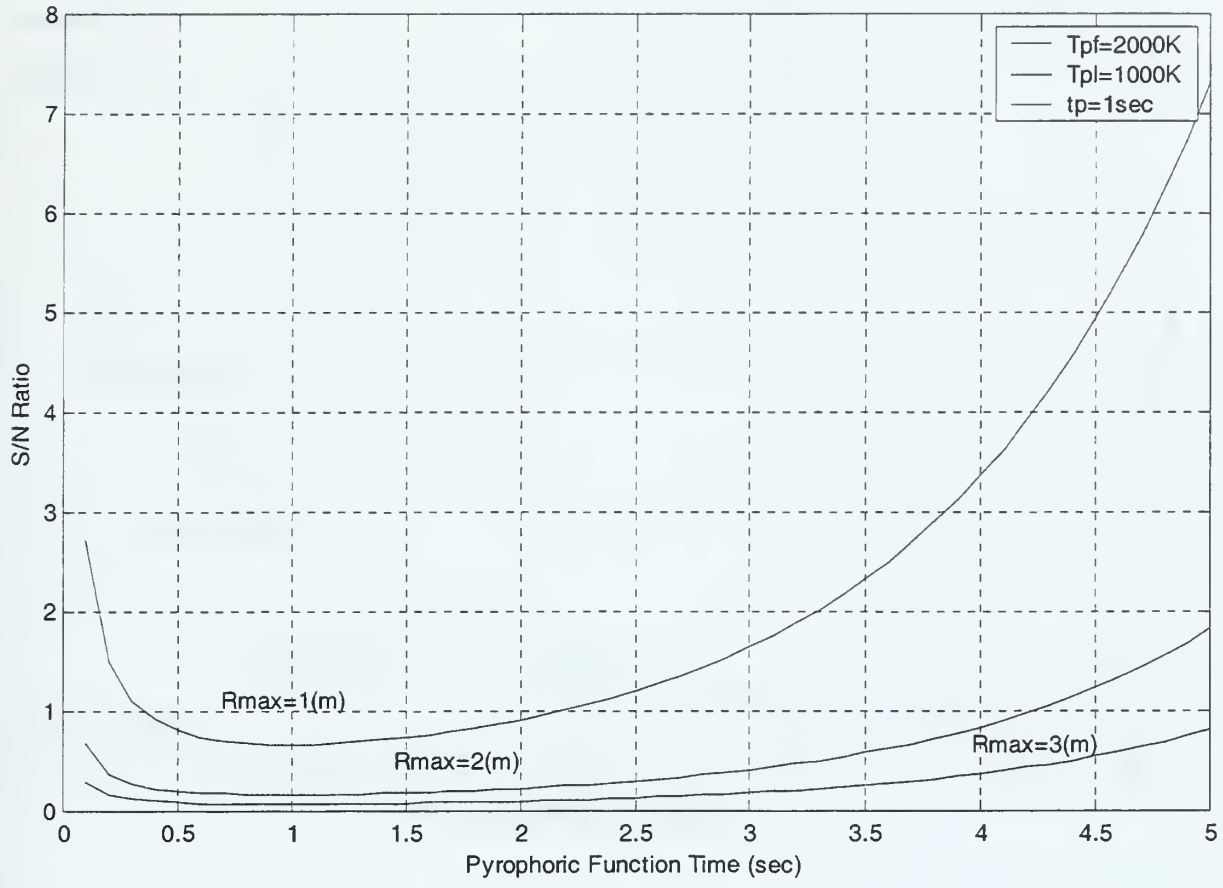

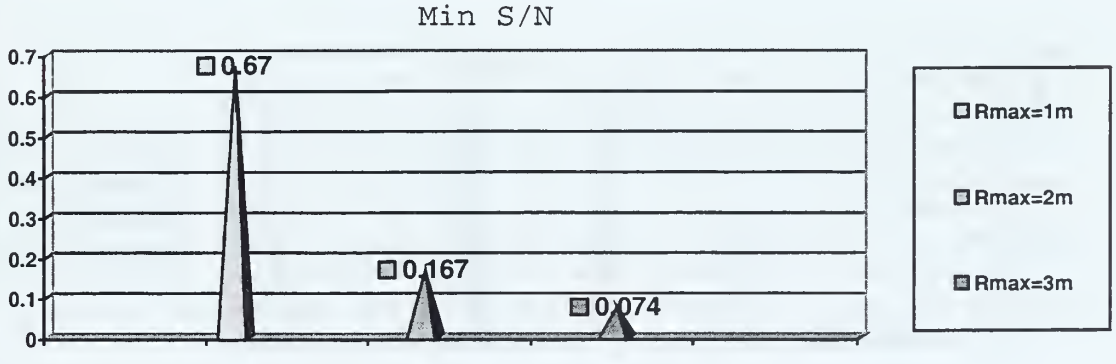

Figure 6.2 S/N for various r_{MAX}

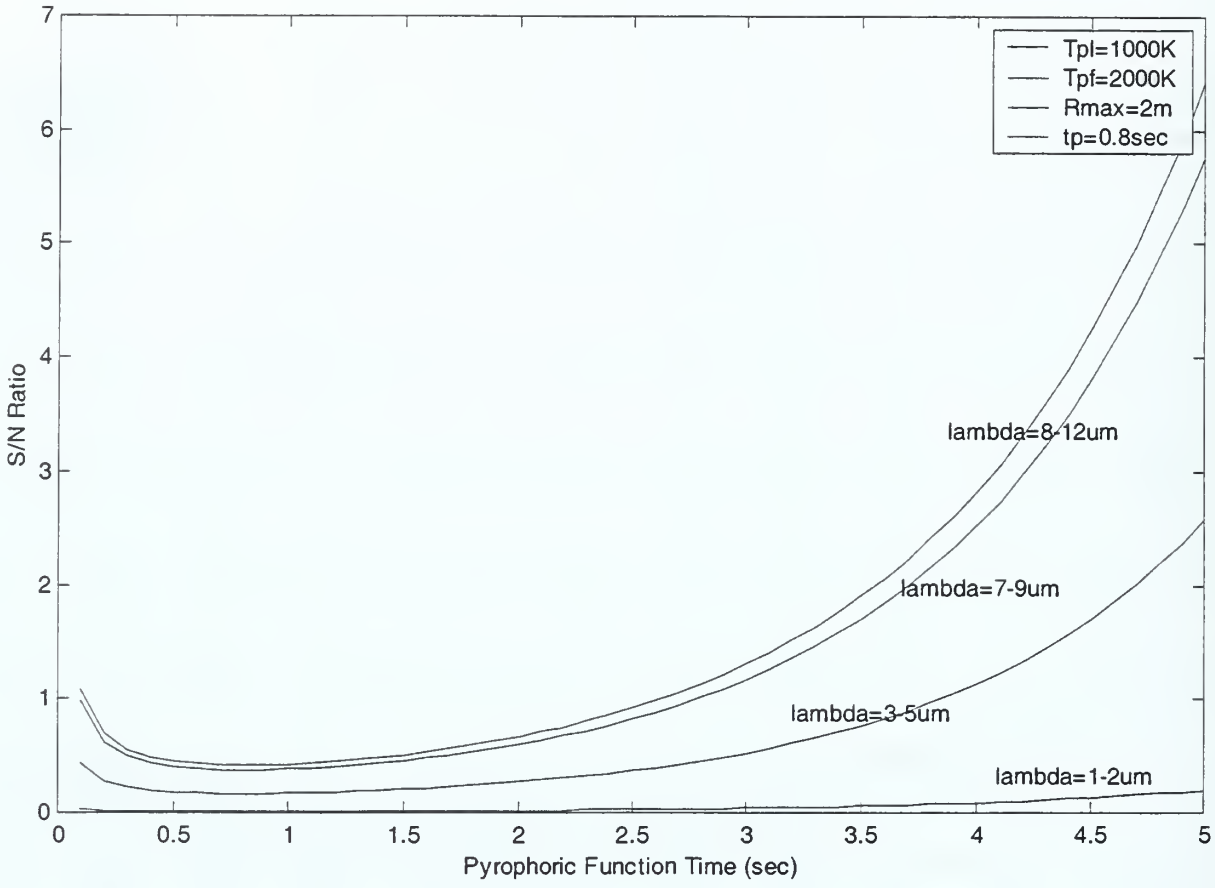

Min S/N

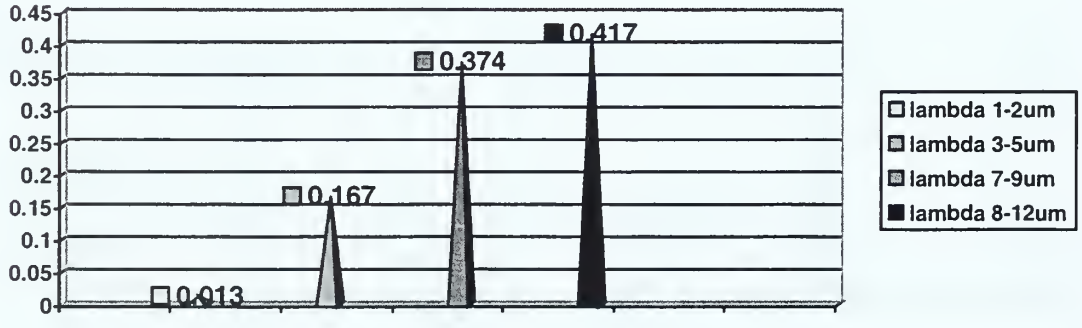

Figure 6.3 S/N for various Detector Bandpass

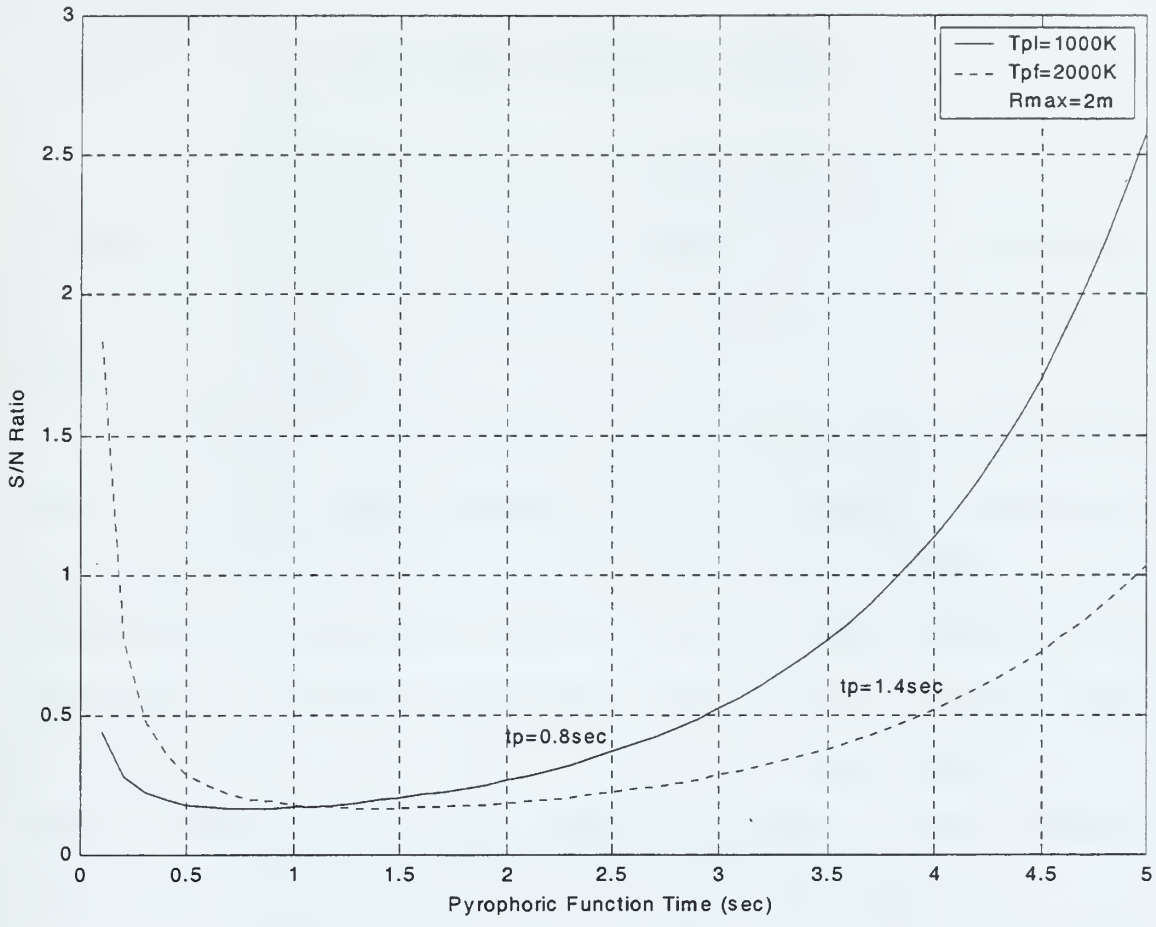

Time period (sec) below 0.5 value of S/N

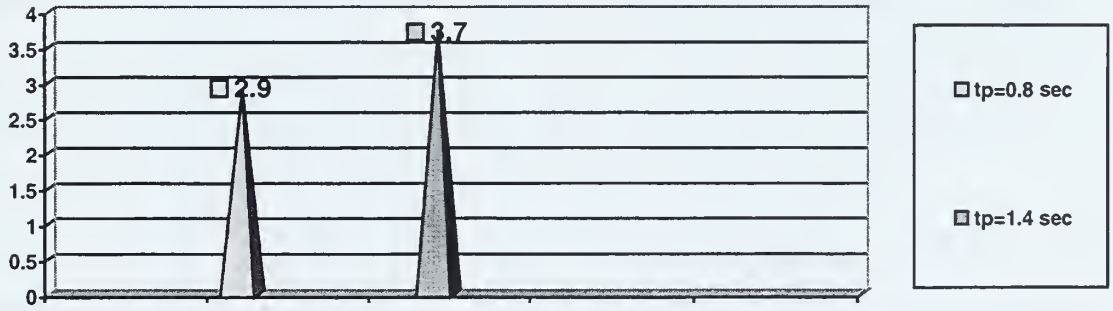

Figure 6.4 S/N for various t_p

VII. PRESENTATION OF IMAGES

The second part of the main program, which is recorded in Appendix B, consists of the generation of the pyrophoric and plume images. The procedure which is followed is described in Chapter V.

The image visualization is created by using a definable number of pixels. The command "image" in **MATLAB** creates an image graphics object by interpreting each element of the pyrophoric or the plume matrix which has been created as an index into the figure's colormap. Each element of the above matrix specifies the color of a rectilinear patch in the image. Along with the command "image", the command "CdataMapping/scaled" is used to scale the values.

The variation in radiant intensity for the pyrophoric image can be described better with two colormaps. The "jet" colormap, which ranges from blue to red and passes through the colors cyan, yellow, and orange. The "gray" colormap returns a linear grayscale colormap. In Figures 7.2 to 7.6, a colorbar is used to show the current color scale.

The second part of the M-file **pyrof.m**, which is recorded in Appendix B, is used to provide image snapshots for different instances of time for the pyrophoric model and for the plume model which is constant with time. For example

see Figure 7.1 which was generated with T_{pi}=1000K. A sequence of pyrophoric images on a "jet" colormap for a pyrophoric with a burn function of seven seconds, burn temperature of T_{pf}=2000K, detector band 3-5 micron band, peak radiant intensity at t_p=1.5 seconds, and radius at t_p equal to two meters are shown in Figures 7.2 through 7.6 for times t=1, t=1.5, t=3, t=5, and t=7 seconds, respectively. Looking at these plots, we observe that the ring with the maximum radiant intensity will be small and close to the center for small times. At the end of the burn, for the pyrophoric flare the circular periphery of peak radiant intensity has a larger size but a lower radiant intensity value.

One byproduct of the time-space modeling of the pyrophoric burn is that the radiant energy profile does not remain peaked at the center. This point was previously made in Chapter III and qualitatively represented with the time dependent graph of Figure 3.8. The images of the pyrophoric flare seen in Figures 7.2 to 7.6 demonstrate this property. This is a byproduct of the assumption that the peak in the radiant intensity will occur for t_p>0 for a spherical "shell" at $r=r_{MAX}$>0. This is consistent with a physical model of an expanding material for which the center burns first and then an outward radial wave of combustion follows.

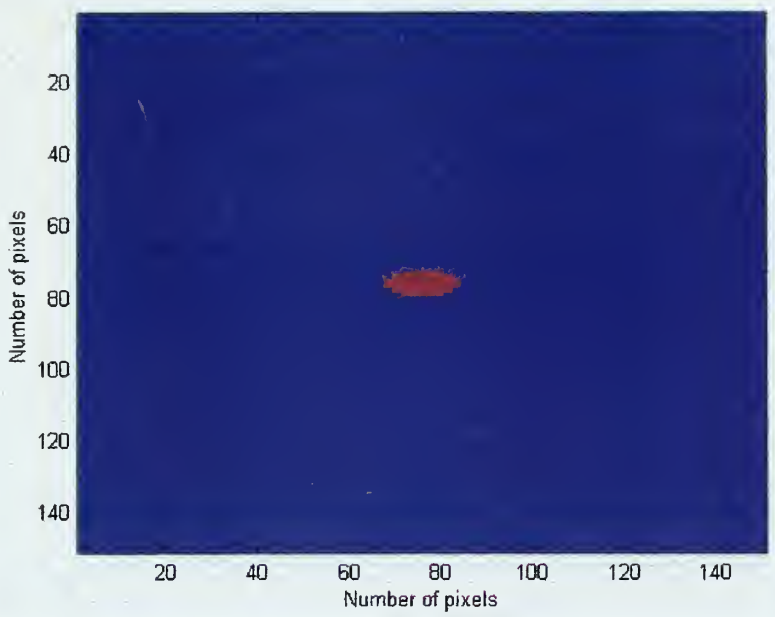

Figure 7.1 The Plume Image.

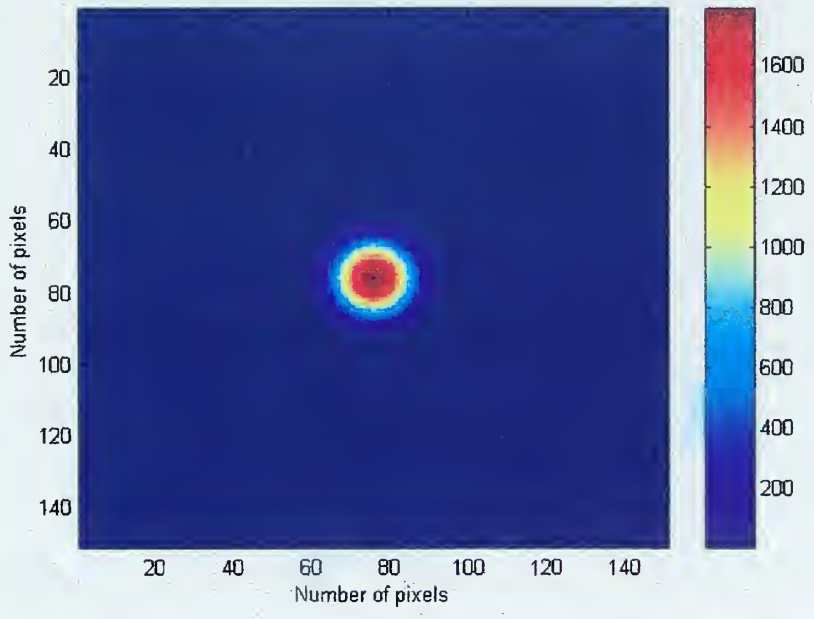

Figure 7.2 The pyrophoric image at t=1 sec.

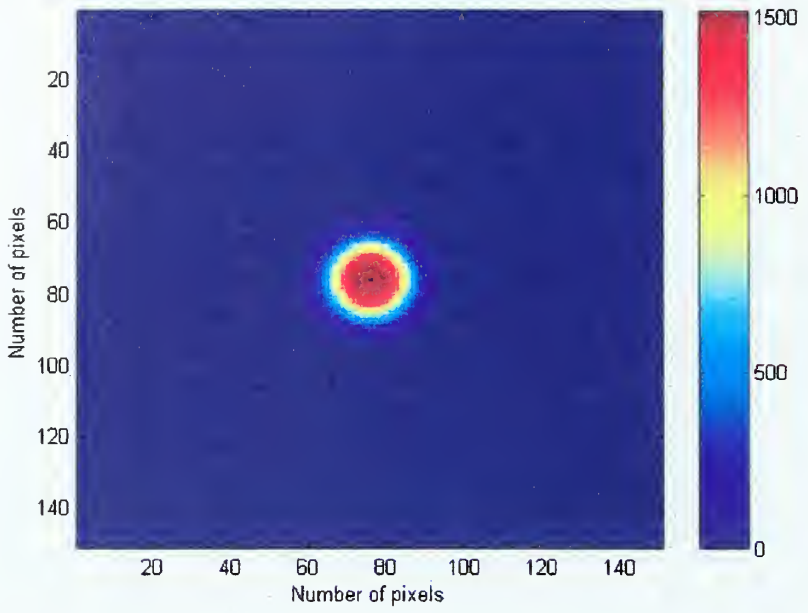

Figure 7.3 The pyrophoric image at $t=t_p=1.5$ sec.

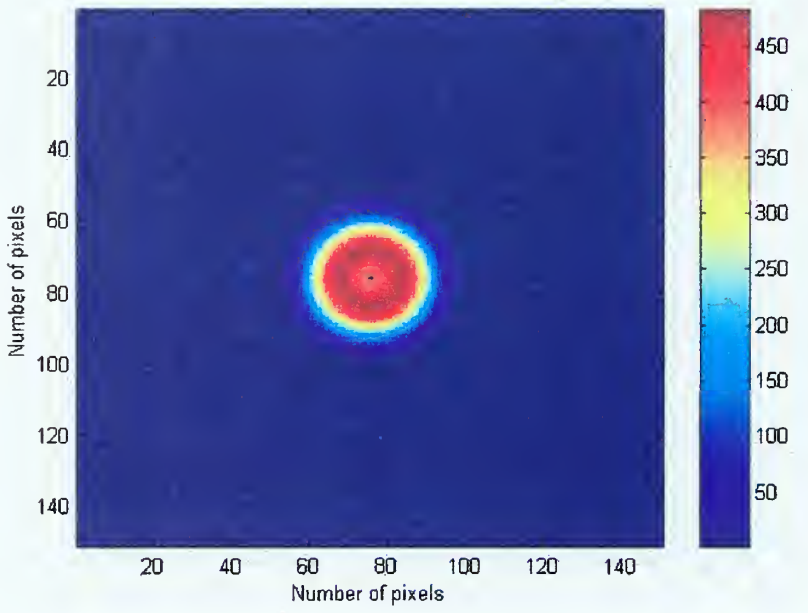

Figure 7.4 The pyrophoric image at t=3 sec.

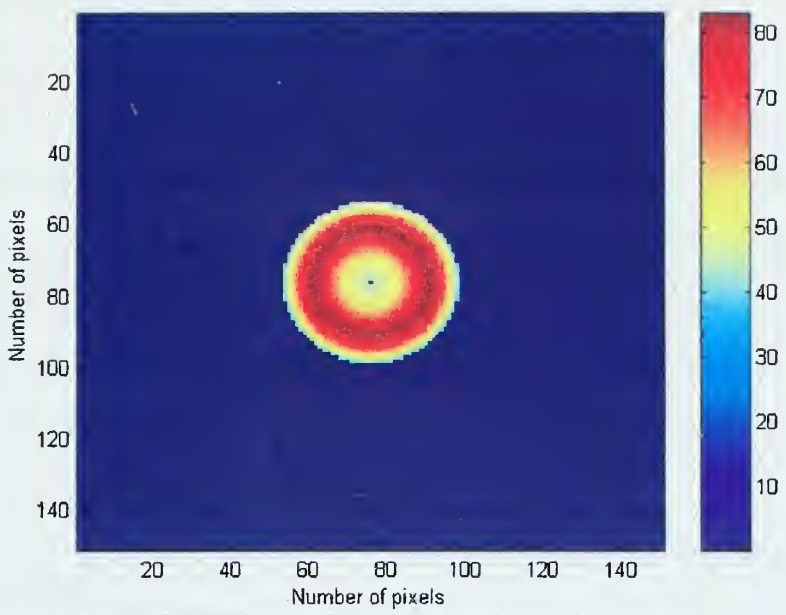

Figure 7.5 The pyrophoric image at t=5 sec.

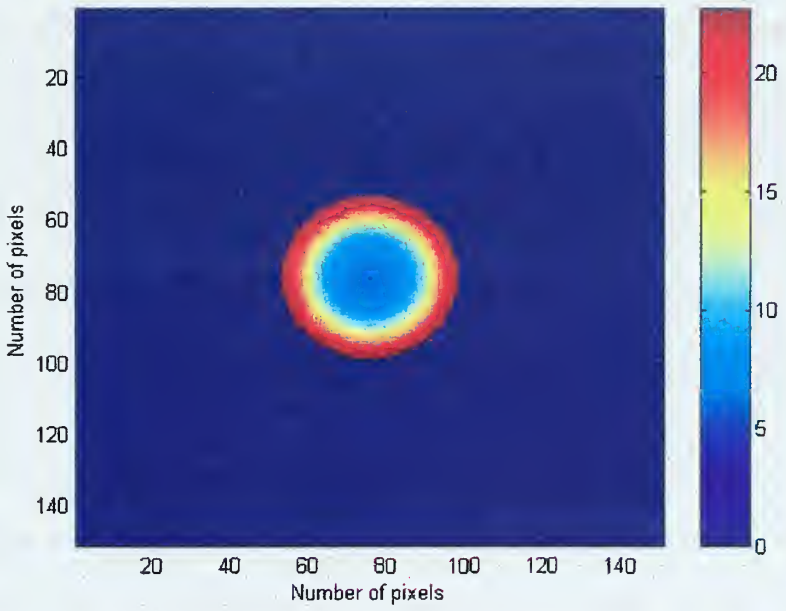

Figure 7.6 The pyrophoric image at t=7 sec.

Representation of the images may give the impression that setting the plume in the center of the pyrophoric image will allow the missile to detect the plume, which is uncovered as the radial wave of combustion moves outward. This is not true since the reticle based detection system, represented in Figure 7.7, converts all the pixels inside the FOV to one value.

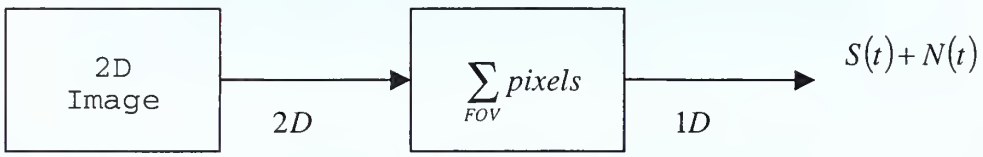

Figure 7.7 Reticle based Detection System.

It should be noted that the S/N predictions in Chapter VI are based on this model. In particular, using a reticle, the missile electro-optic (EO) process converts two-dimensional (2D) optical image to a one-dimensional (1D) electronic signal [Ref 1].

VIII.MULTIPLE PYROPHORIC FLARES

The main computer program code also simulates the dropping of multiple pyrophoric flares, each at different instances of time and with generally different parameters. These parameters include pyrophoric temperature, T_{pf}, radius of pyrophoric at the peak radiant intensity, $r_{MAX,}$ and the time of peak radiant intensity, t_p.

Using this option, a scenario can be generated where a pre-launched unmanned tactical air launched decoy (TALD) drops a sequence of flares in advance of a manned aircraft. The missile will then be distracted by a flare generated IR noise curtain. The intent is to provide 'cover' to the manned aircraft which flies into a safe-zone corridor a few seconds later. This is represented in Figure 8.1.

The settings on the different parameters of the ejected pyrophoric can be chosen according to the conclusions reached from studying Figures 6.1, 6.2, and 6.4 in Chapter VII. In particular, an increase in the pyrophoric temperature T_{pf} or an increase in the radius r_{MAX} significantly decreases S/N between the initial and final time of the pyrophoric function. Also, a flare which achieves peak radiant intensity at a later point in time will have an extended window of effectiveness.

The radiant intensity for four pyrophoric flares, which have a function burn time of 5s and are launched at times t=0s, t=0.5s, t=1s, and t=1.5s are shown in Figure 8.2. The first flare has the shortest time to peak radiant intensity, t_p=0.8s. This value is selected in order to capture the missile seeker quickly. Other specifications for the first flare include r_{MAX}=2m and T_{pf}=2200K, which were chosen to keep S/N low. The second and third flares, which are launched at t=0.5s and t=1s, respectively, have a longer time to reach peak radiant intensity, t_p=1.2s, in order to create an extended window of effectiveness. For these two flares, r_{MAX}=1m and T_{pf}=2000K are used. These have been selected lower relative to r_{MAX} and T_{pf} for the first flare since there is still significant radiant energy from the first flare. The last flare is launched at t=1.5s with larger values of r_{MAX} and T_{pf} relative to the previous two flares, r_{MAX}=2m and T_{pf}=2200K. Higher values are used in order to maintain a low value of S/N by compensating for the reduction in effectiveness of the first flare. In addition, t_p=1.2s is used in order to have an extended window of effectiveness.

The composite radiant intensity of the four flares versus the total function burn time is shown in Figure 8.3. The changes in slope are correlated with the activation of new flares.

The composite S/N versus the total function burn time is represented in Figure 8.4. Also, in this plot the changes in slope are correlated with the activation of new flares.

The S/N curves that correspond to each flare are shown in Figure 8.5. By comparing Figure 8.4 and Figure 8.5, it is obvious there is an extension of the length of time S/N remains below some threshold (e.g., 0.5) with the use of multiple flares. This point is quantified in Table 8.1.

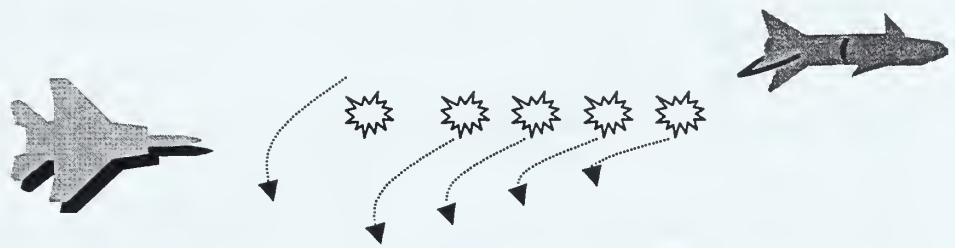

Figure 8.1 Pre-launched Unmanned Tactical Air Launched Decoy (TALD) drops a Sequence of Flares in advance of a Manned Aircraft.

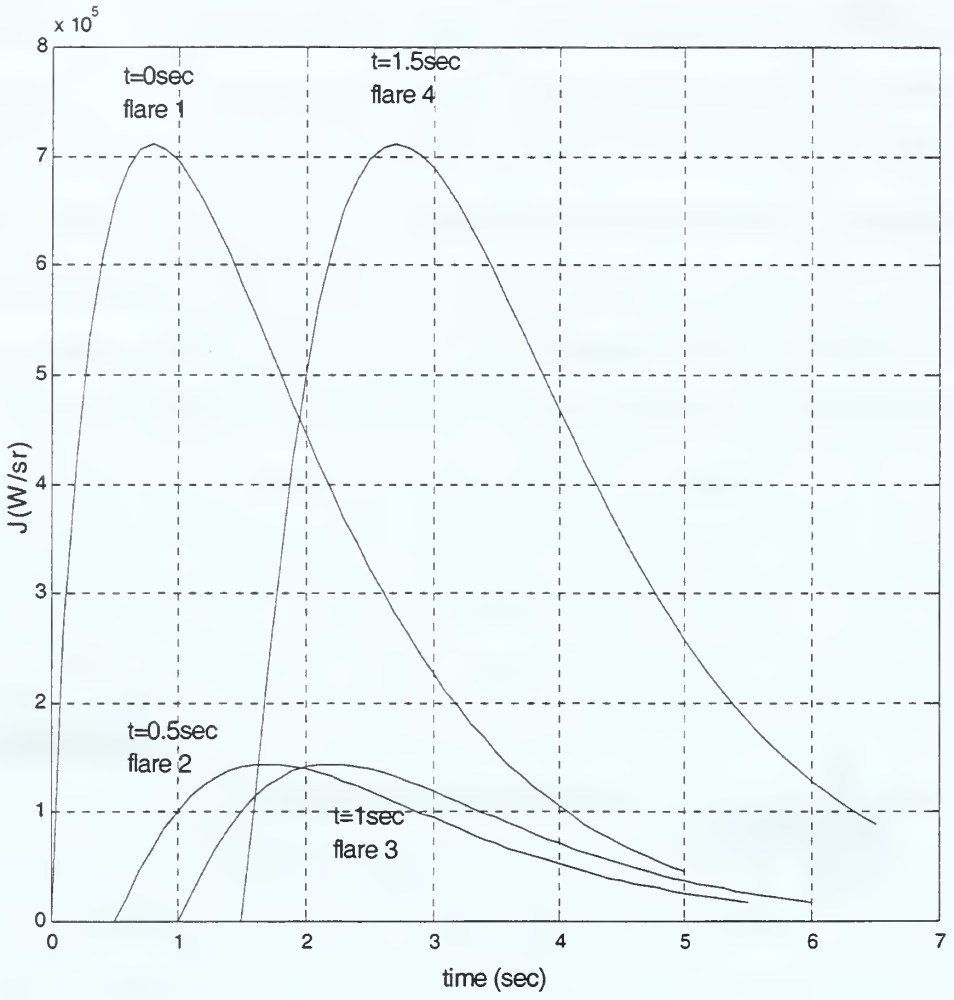

Figure 8.2 The Radiant Intensity Distribution of the four Pyrophorics.

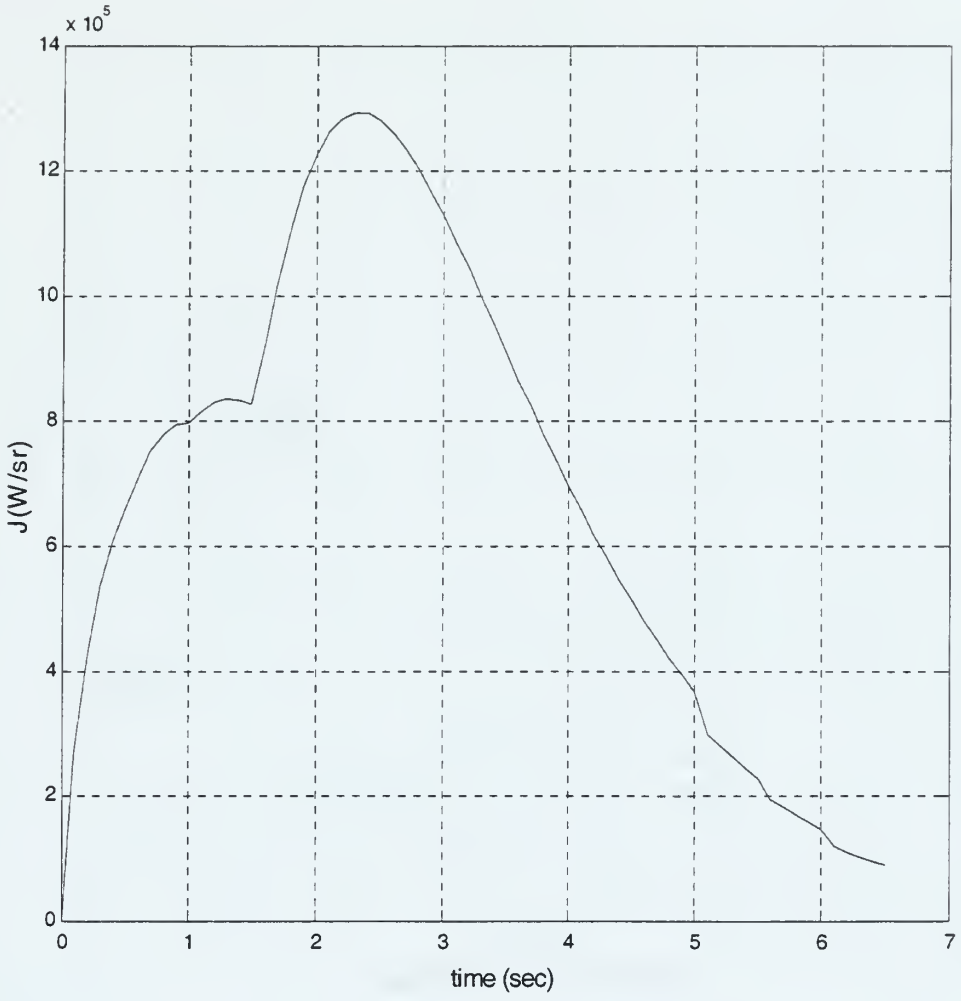

Figure 8.3 The Composite Radiant Intensity Distribution of the four Pyrophorics.

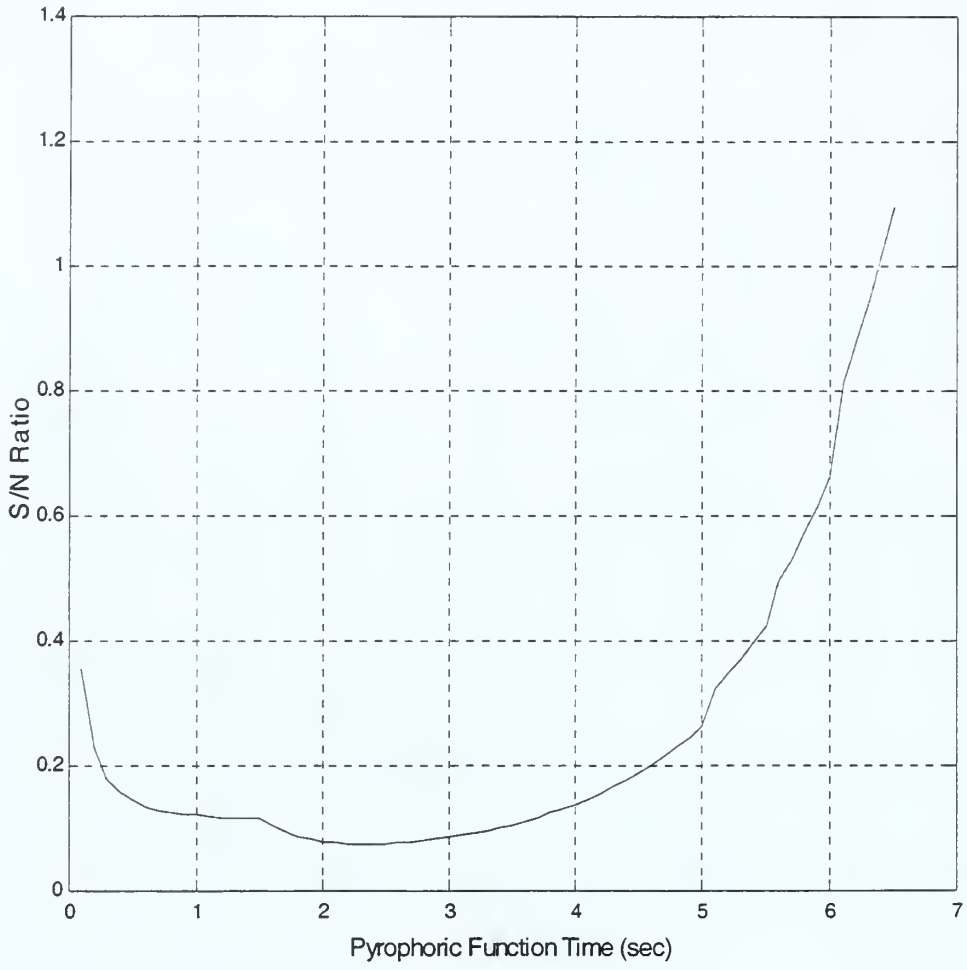

Figure 8.4 The Composite S/N versus the Total Function Burn Time.

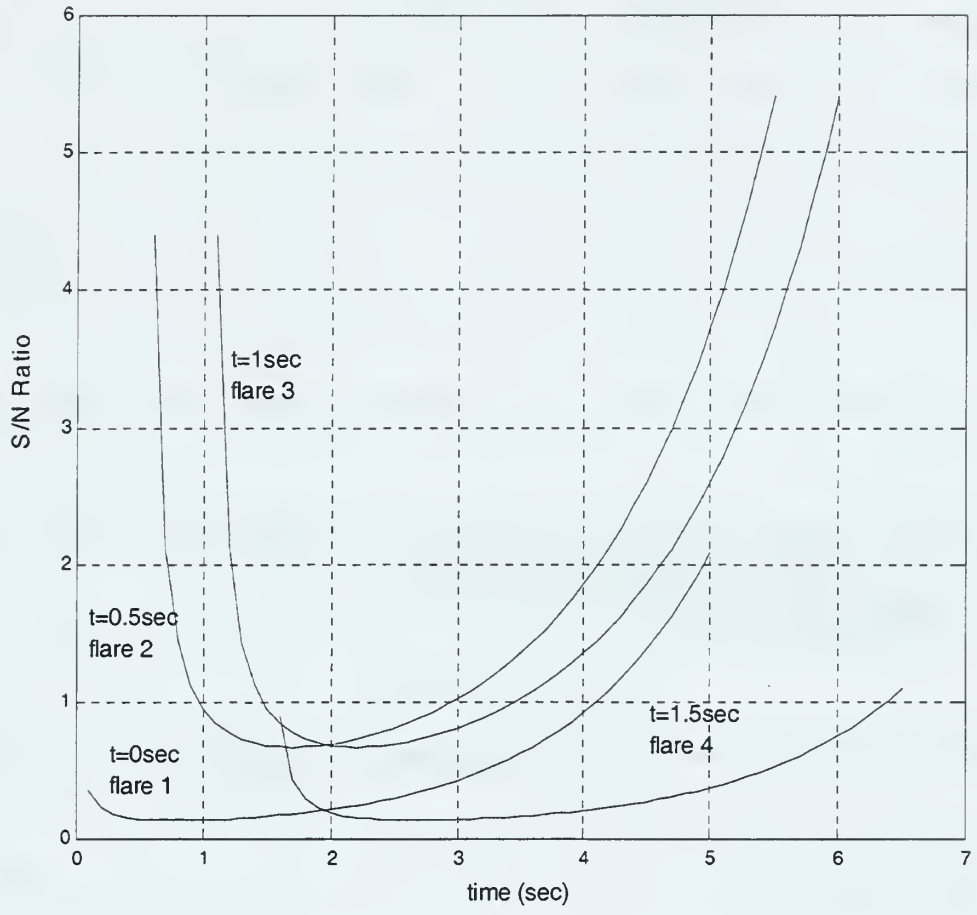

Figure 8.5 S/N ratio Curves for Each Flare.

Table 8.1 Time below the 0.5 threshold.

Flare number	Time below the 0.5 threshold (sec)
Flare 1	~3
Flare 2	0
Flare 3	0
Flare 4	~3
Composite flare	~5.5

In order to demonstrate how these results apply to tactical decisions that need to be made in the field, two examples are presented. The conditions that the manned aircraft be given safe cover while being viewed by a "stationary missile" can be stated as

$$\Delta t_{S/N} \geq t_{dac} + R_f / V_{ac} \qquad (VIII-1)$$

where

-$\Delta t_{(S/N)}$ is the time S/N is depressed below a specified threshold

-t_{dac} is the approximate time after the dropping of the first flare that the aircraft enters the safe corridor

-V_{ac} aircraft velocity

Equation (VIII-1) can be rearranged as follows:

$$\frac{V_{ac}}{R_f} \geq \left[\frac{1}{\Delta t_{S/N} - t_{dac}} \right] \qquad (VIII-2)$$

For convenience of interpretation, minimum values for (V_{ac}/R_f) are plotted in Figure 8.6 versus $\Delta t_{(S/N)}$ for various values in the time delay, t_{dac}.

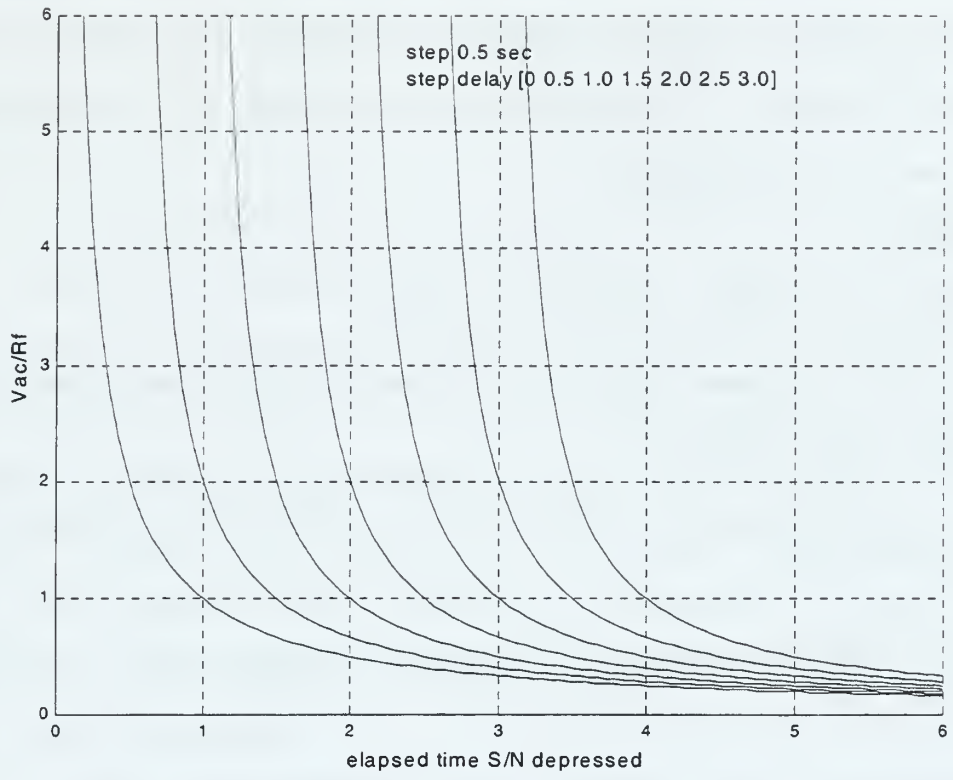

Figure 8.6 Minimum Velocity Curves for various Values of Time Delay Parameter.

Example 1

Given V_{ac}=186 m/sec(≈0.56 MACH1), R_f=62 m, t_{dac}=1.0s, what is the minimum allowed time to keep S/N depressed in order to provide "safe" cover?

Step 1 Calculate $V_{ac}/R_f \approx 3s^{-1}$

Step 2 For delay t_{dac}=1.0s, read from Figure 8.6, 1.5s.

From the above graph and reference to Table 8.1, it is obvious that any one of the flares studied would be

sufficient. However, if the aircraft delay is changed to 3.0 seconds and V_{ac}=62 m/sec, then the condition on minimum $\Delta t_{(S/N)}$ changes to about 4.1 seconds and more than one flare packet will need to be dropped.

Example 2

Given $\Delta t_{(S/N)}$=2s, R_f=62 m, t_{dac}=1.5s,

what is the minimum velocity of the aircraft in order to be provided "safe" cover?

Step 1 For $\Delta t_{(S/N)}$=2s and t_{dac}=1.5s, read from Figure 8.6, $(V_{ac}/R_f)_{min} \approx 2.0 s^{-1}$

Step 2 Use the results from step 1 with R_f=62 m to obtain $(V_{ac)MIN}$=124 m/sec(≈37% MACH1)

The point of this example is to demonstrate that a time limit in the required reduction of S/N forces a predictable lower limit on the velocity of the manned aircraft.

From Figures 8.4 and 8.6 several significant and general observations can be deduced. First, because the period of time in which S/N stays below a given threshold is finite, as can been seen from Figure 8.4, there is an upper limit on the delay that can take place before the manned aircraft enters the safe corridor. The longest this delay can be is the total time interval that S/N is below the threshold. Note from Figure 8.6 that each curve predicts the minimum required velocity of aircraft which approaches infinity as the elapsed time for S/N to be depressed

asymptotically approaches the delay. For example, the curve with a delay of three seconds approaches infinity from the right as the elapsed time S/N depressed approaches three seconds.

These curves predict in general that a greater delay in the aircraft entering the corridor requires a greater velocity of the manned aircraft in order to guarantee safe passage. Conversely, the curves when applied in reverse suggest a minimum required time for the depression in S/N. In particular, from Figure 8.6 it follows that the greater the delay and/or the slower the velocity of the manned aircraft, the longer S/N needs to stay depressed below a specified threshold.

IX. CONCLUSIONS AND FUTURE ENHANCEMENTS

The objective of this research was to model the impact of dropping pyrophoric type flares which are in the field-of-view of a prelaunch missile. It is assumed that these flares are launched from an unmanned tactical air launched decoy (TALD). The manned aircraft, which needs protective cover and will presumably benefit from the flares, will follow into the corridor a few seconds after the start of the flare sequence.

In order to reach this objective, a simulation model of the time-space radiant intensity distribution for a pyrophoric flare expendable has been developed. The performance of the pyrophoric flares to create a distraction for the missile was characterized in term of S/N where S is the radiant power of the plume and N is the radiant power of one or more flares. Several conclusions from this study are described in the next two paragraphs.

The radiant power for the pyrophoric flare burn in the [3-5] micron band was found to be significantly higher than what occurs in the [8-12] micron band. It was also found that increasing the pyrophoric temperature T_{pf} or increasing the radius r_{MAX} significantly decreases S/N between the initial and final time of the pyrophoric function. Finally, a flare which achieves a peak radiant intensity later in

time has an extended window of effectiveness; i.e., a longer window in time for which S/N remains below a specified threshold.

In this thesis the concept of dropping of multiple pyrophoric flares to create a "safe" corridor for manned aircraft missions was evaluated. In particular, multiple flare "packets" lengthen the window over which S/N remains below an acceptable threshold.

Lastly, it was noted that if the manned aircraft is not moving with high enough velocity there will be a problem in generating "safe" cover. From this concept, a rule relating minimum aircraft velocity to both the delay in entering the safe corridor and the time S/N is depressed was presented and illustrated with several examples.

A number of simplifying assumptions were applied in the study. Future work on the simulation model could focus on one or more of these assumptions. For example, to mention a few points, atmospheric absorption was neglected in this study. Also, the plume was assumed to be a constant temperature graybody. A better model for the atmospheric absorption would be to consider the cold CO_2 absorption spectrum. For the plume, consideration of the hot CO_2 emission spectrum would be also beneficial (the red spike-blue spike effect). Also, an experimental data based model for the pyrophoric burn radiation spectrum could be used to

refine the simulation model. Finally, the calculations of S/N could be based on more complex image processing algorithms that are indicative of modern reticle based missiles.

APPENDIX A. COMPUTER AND ANALYSIS VARIABLES

Computer Variables	Analysis Variables	Brief Description
FOV	FOV	Missile field-of-view
R	R	Range between missile and target
Rfield	R_{Field}	Range inside missile's field-of-view on target's plane
Tpf	T_{pf}	Pyrophoric temperature
Tpl	T_{pl}	Plume temperature
lambda1	λ_1	Initial wavelength
lambda2	λ_2	Final wavelength
t1	t_1	Initial time of pyrophoric function
t2	t_2	Final time of pyrophoric function
t_peak	t_p	Pyrophoric time at max radiant intensity
r_max_t	r_{MAXt}	Radius of pyrophoric

rmax	r_{MAX}	Radius of pyrophoric at max radiant intensity
rnorm	r_{NORM}	Normalization radius of pyrophoric
Afl	A_{fl}	Area of pyrophoric at max radiant intensity
Apl	A_{pl}	Area of plume
a	a_{pl}	Major axis of plume's ellipse area
b	b_{pl}	Minor axis of plume's ellipse area
vel	u_p	Velocity of pyrophoric
e	e	Average emissivity
s	σ	Stefan-Boltzmann constant
Wflare	$W(\lambda,T)_{pf}$	Total emittance of pyrophoric
Wplume	$W(\lambda,T)_{pl}$	Total emittance of plume
Wpfb	$W(\lambda_1,\lambda_2)_{pf}$	Emittance of pyrophoric in the band of interest
Wplb	$W(\lambda,\lambda_2)_{pl}$	Emittance of plume in the band of interest
ratWfl	η_{pf}	Fraction of pyrophoric emittance in the band of interest

ratWpl	η_{pl}	Fraction of plume emittance in the band of interest
J_max	J_{MAX}	Peak radiant intensity of pyrophoric
J	J(t)	Radiant intensity of pyrophoric function
Jpfb	$J(\lambda_1,\lambda_2)_{pf}$	Radiant intensity of pyrophoric in the band of interest
Jplb	$J(\lambda_1,\lambda_2)_{pl}$	Radiant intensity of plume in the band of interest
fa	f(t,a)	Gamma distribution
G	$\Gamma(a)$	Gamma function
a	a	Parameter (a) of Gamma Distribution
fad	$f(x;\mu,\sigma)$	Gaussian space distribution
s	σ	Standard deviation of Gaussian distribution
m	μ	Mean of Gaussian distribution
Q	Q	Amount under a Gaussian distribution curve
scrJ	$j(r_{NORM},t/t_p)$	Weighted value of a Gaussian distribution in normalized space domain
Intscr	$J_v(r_o,t)$	Integrated view radiant intensity
Npix	N'_{pix}	Number of pixels
Cpf	C_{ij}	Pyrophoric image matrix

Cpl	C_{ij}	Plume image matrix
Cpfn	C'_{ij}	Normalized pyrophoric image matrix
Cpln	C'_{ij}	Normalized plume image matrix
Ratio	S/N	S/N ratio

APPENDIX B. MATLAB CODES

This appendix contains listing of all **MATLAB** input files that were used to get the results posted in Chapters VI,VII and VIII. These M-files are:

1. **Pyrof.m,**
2. **Plankpf.m**
3. **Plankpl.m**
4. **Dquad1.m**
5. **Dquad1.m, and**
6. **Gammaz.m**

Pyrof.m is the main computer code which has two parts. The first part generates the S/N curves for one or multiple pyrophoric with different parameters and the second part generates the pyrophoric and plume images.

Plankpf.m is a function file which calculates the Spectral Radiant Emittance (SRE) for the pyrophoric at temperature T_{pf} (Kelvin).

Plankpl.m is a function file which calculates the Spectral Radiant Emittance (SRE) for the plume at temperature T_{pl} (Kelvin).

Dquad1.m is a function file which calculates the Spectral Radiant Emittance (SRE), for the plume at temperature T_{pl}(Kelvin), inside the detectors band.

Dquad2.m is a function file which calculates the Spectral Radiant Emittance (SRE), for the pyrophoric at temperature T_{pf}(Kelvin), inside the detectors band.

Gammaz.m is a function file which calculates the GAMMA function.

Program 1 Pyrof.m

```
  %%%%%%%%%% MAIN COMPUTER CODE %%%%%%%%%%
%%%%Ref. files:
                % plankpf.m, plankpl.m,
          % dquad1.m, dquad2.m,  gammaz.m

format long

global Tpl
global lambda1
global lambda2
global Tpf
global t1
global t2

%%%%% Inputs %%%%

program=input('For the S/N part enter 1, else for the images part enter
2 :');
%%%%%%%%%%%%%%%%%%%% First Part
if program==1
Tpl=input('Set the  Temperature of plume (Kelvin): ');
Tp=input('Set the Temperature of Pyrophoric (Kelvin): ');
lambda1=input('Set the value of the lambda1 (um): ');
lambda2=input('Set the value of the lambda2 (um): ');
t1=input('Set the initial value of the time for the Pyrophoric  (sec):
');
t2=input('Set the final value of the time for the Pyrophoric(sec): ');
t_peak1=input('Set the  value of the t_peak (sec): ');
rmaxp=input('Set the  value of the rmax (m): ');
t3=input('Set the increment step between t1 and t2: ');
tfl=input('Set the dropped times of pyroforic: ');

t=t1:t3:t2;
figure(1)
for z=1:length(tfl);
   tflare=tfl(z);
   if length(t_peak1)==1;
      t_peak=t_peak1;
   else
      t_peak=t_peak1(z);
   end
   if length(Tp)==1;
      Tpf=Tp;
   else
      Tpf=Tp(z);
   end
   if length(rmaxp)==1;
      rmax=rmaxp;
   else
      rmax=rmaxp(z);
   end

e=0.9;  %emissivity of Pyrophoric
s=5.67*10^(-12);% Stefan-Boltzmann constant (cm)
```

```
Wpfb=dquad2('plankpf',lambda1,lambda2);%Emittance between the two lambda
%( W cm^(-2) )
Wflare=s*Tpf^4; %Stefan-Boltzmann(total emittance over all wavelengths)
Afl=4*pi*(rmax)^2; % Area Pyrophoric at t_peak
s1=5.67*10^(-8);% Stefan-Boltzmann constant (m)
J_max=((e*s1*Tpf^4)/(4*pi))*Afl; % Total Radiant Intensity(W/sr)
ratWfl=(Wpfb/Wflare);

m=(tflare/t3)+1;
a=t_peak+1;
G=gammaz(a); % Find 'G' with the help of 'gammaz' function
fa=(t.^(t_peak).*exp(-t))./G;% gamma equation
J=(fa.*J_max)*(1/max(fa)); % Normalized to the total Radiant Intensity
%J_max
Js=J*ratWfl;
[r1,r2]=size(Js);
c1=Js(1,2:r2);
c=[zeros(1,m),c1];
if z==1;
      y=1:length(c);
      y=c;
else
      y=[y,zeros(1,(length(c)-length(y)))]+c;
end
tpl=0:t3:((length(c)-1)*t3);
eval(['save data',num2str(z),'.mat']);
eval(['load data',num2str(z),'.mat']);
plot(tpl,c)
grid on
xlabel('time (sec)')
ylabel('J(W/sr)')
hold on
end

figure(2)
tcomp=0:t3:((length(y)-1)*t3);
plot(tcomp,y)
grid on
xlabel('time (sec)')
ylabel('J(W/sr)')

% Calculation of radiant intensity for the plume
Wplb=dquad1('plankpl',lambda1,lambda2);%Emittance between the two lambda
%( W cm^(-2) )
a=1.50; %minor axis (m)
b=3.50;  %major axis (m)
Apl=pi*a*b; %(Area)
e=0.9;  %emissivity
s=5.67*10^(-12); %Stefan-Boltzmann constant
Wplume=s*Tpl^4; %Stefan-Boltzmann(total emittance over all wavelengths)
s1=5.67*10^(-8);% Stefan-Boltzmann constant (m)
ratWpl=Wplb/Wplume;
Jpl=((e*s1*Tpl^4)/pi)*Apl*ratWpl; %Radiant Intensity between the two
%lambda(W/sr)
Jplume=Jpl.*ones(1,length(y));

% ********* S/N Ratio *******
Ratio=Jplume./y;

figure(3)
plot(tcomp,Ratio)
```

```
grid on
xlabel(' Pyrophoric Function Time (sec) ')
ylabel('S/N Ratio')

figure(4)
for x=1:length(tfl);
    tflare=tfl(x);
   if length(t_peak1)==1;
      t_peak==t_peak1;
   else
      t_peak=t_peak1(x);
   end
   if length(Tp)==1;
      Tpf==Tp;
   else
      Tpf=Tp(x);
   end
   if length(rmaxp)==1;
      rmax==rmaxp;
   else
      rmax=rmaxp(x);
   end

% Calculation of radiant intensity for the pyrophoric
e=0.9;  %emissivity of Pyrophoric
s=5.67*10^(-12);% Stefan-Boltzmann constant (cm)
Wpfb=dquad2('plankpf',lambda1,lambda2);%Emittance between the two lambda
%( W cm^(-2) )
Wflare=s*Tpf^4; %Stefan-Boltzmann(total emittance over all wavelengths)
Afl=4*pi*(rmax)^2; % Area Pyrophoric at t_peak
s1=5.67*10^(-8);% Stefan-Boltzmann constant (m)
J_max=((e*s1*Tpf^4)/(4*pi))*Afl; % Total Radiant Intensity(W/sr)
ratWfl=(Wpfb/Wflare);

m=(tflare/t3)+1;
a=t_peak+1;
G=gammaz(a); % Find 'G' with the help of 'gammaz' function
fa=(t.^(t_peak).*exp(-t))./G;% gamma equation
J=(fa.*J_max)*(1/max(fa)); % Normalized to the total Radiant Intensity
%J_max
Js=J*ratWfl;
[r1,r2]=size(Js);
c1=Js(1,2:r2);
c2=[zeros(1,m),c1];
Jplume=Jpl.*ones(1,length(c2));
c=Jplume./c2;
tpl=0:t3:((length(c)-1)*t3);

eval(['save datas',num2str(x),'.mat']);
eval(['load datas',num2str(x),'.mat']);
plot(tpl,c)
grid on
xlabel('time (sec)')
ylabel('S/N Ratio')
hold on
end
%%%%%%%%%%%%%%%%%%%% Second Part
else
Npix=input('Set the number of pixels (it must be an integer value with
half an odd number): ');
tspf=input('Set the time (sec) that you want to create the images: ');
```

```
Tpl=input('Set the  Temperature of plume (Kelvin): ');
Tpf=input('Set the Temperature of Pyrophoric (Kelvin): ');
lambda1=input('Set the value of the lambda1 (um): ');
lambda2=input('Set the value of the lambda2 (um): ');
t1=input('Set the initial value of the time for the Pyrophoric  (sec):
');
t2=input('Set the final value of the time for the Pyrophoric(sec): ');
t_peak=input('Set the  value of the t_peak (sec): ');
rmax=input('Set the  value of the rmax (m): ');
t3=input('Set the increment step between t1 and t2: ');

% Calculation of radiant intensity for the plume
Wplb=dquad1('plankpl',lambda1,lambda2);
a=1.5; %minor axis (m)
b=3.5;  %major axis (m)
Apl=pi*a*b; %(Area)
e=0.9;  %emissivity
s=5.67*10^(-12); %Stefan-Boltzmann constant
Wplume=s*Tpl^4; %total emittance over all wavelengths
s1=5.67*10^(-8);% Stefan-Boltzmann constant (m)
Jplb=((e*s1*Tpl^4)/pi)*Apl*(Wplb/Wplume); %Radiant Intensity between the
%two lambda(W/sr)

FOV=((pi*2)/180);
Range=1.8*(10^3); %(m)
Rfield=FOV*Range; %(m)

%I create the image matrix for the Plume
Cpl=zeros(Npix+1,Npix+1);
for i1=-Npix/2:1:Npix/2;
   for j1=-Npix/2:1:Npix/2;
      ipix1=i1+((Npix/2)+1);
      jpix1=j1+((Npix/2)+1);
      r1=((i1).^2./(a/Rfield)^2)+((j1).^2./(b/Rfield)^2);
      if r1<=(Npix+1)^2;
         Cpl(ipix1,jpix1)=Jplb;% I assign the value Jplb to the pixels
%inside the matrix
      else
         Cpl(ipix1,jpix1)=0;% I assign the value 0 to the pixels outside
%the matrix

      end
   end
end
sum1=0;
for i=1:(Npix+1);
   for j=1:(Npix+1);
      sum1= sum1+ Cpl(i,j);
   end
end
newCpl= Cpl/sum1 *Jplb;
Cpln=newCpl;

% Calculation of radiant intensity for the pyrophoric
e=0.9;  %emissivity of Pyrophoric
s=5.67*10^(-12);% Stefan-Boltzmann constant (cm)
Wpfb=dquad2('plankpf',lambda1,lambda2);%Emittance between the two lambda
%( W cm^(-2) )
Wflare=s*Tpf^4; %total emittance over all wavelengths
Afl=4*pi*(rmax)^2; % Area Pyrophoric at t_peak
s1=5.67*10^(-8);% Stefan-Boltzmann constant (m)
```

```
J_max=((e*s1*Tpf^4)/(4*pi))*Afl; % Total Radiant Intensity(W/sr)
ratWfl=(Wpfb/Wflare);

t=t1:0.1:t2;
vel=rmax./t_peak;
r_max_t=t.*vel;
rnorm=r_max_t/rmax;

% I create the time distribution(gamma distribution)for a=t_peak+1
a=t_peak+1;
G=gammaz(a); % Find 'G' with the help of 'gammaz' function
fa=(t.^(t_peak).*exp(-t))./G;% gamma equation
J=(fa.*J_max)*(1/max(fa)); % Normalized to the total Radiant Intensity
%J_max


% I create the normalized space distribution
s=1;  % standard deviation
for tx=t1:t3:t2;
 fad=(exp(-(rnorm-(tx/t_peak)).^2./(2*s^2))./(sqrt(2*pi)*s)); %Gaussian
%distribution
 l2=tx;
 fa2=(l2^(t_peak)*exp(-l2))/gammaz(t_peak+1);
 J2=(fa2*J_max)*(1/max(fa)); %  Normalized to the total Radiant
%Intensity J_max
 Q2=(0.5).*erfc((-tx/(t_peak*s))./sqrt(2)); % Integral from zero to
%infinity for a Gaussian distribution with mean at tx/t_peak
scrJ1=fad*J2/Q2; %The weighted values for every Gaussian distribution
%with mean at tx/t_peak
 end

for z=1:length(tspf);
ts=tspf(z);
fay=(exp(-(rnorm-((ts/t_peak))).^2./(2*s^2))./(sqrt(2*pi)*s));
ls=ts;
fas=(ls^(t_peak)*exp(-ls))/gammaz(t_peak+1);
Js=(fas*J_max)*(1/max(fa));
Qs=(0.5).*erfc((-ts/(t_peak*s))./sqrt(2));
scrJ3=fay*Js/Qs;

%I create the integrated Pyrophoric model
Np=30;
[r1,c1]=size(rnorm);
romax=max(rnorm);
Nro=c1-1;
Intscr2=1:Nro+1;
ro=1:Nro+1; % ro is the distance from the center of projection
Dro=romax/Nro;
for J=1:Nro+1;
   sum=0;
   ro(J)=(J-1).*Dro; % for every J pick up one ro
   xmax=sqrt((romax).^2-(ro(J)).^2);
   Dx=xmax./Np;
   for n=1:Np+1;
      x=(n-1).*Dx;
      r=sqrt(x.^2+(ro(J)).^2);
      k1=(r./max(rnorm))*c1;
      k=round(k1);    % index k goes to closest integer
       if k>c1
         a=0;
         sum=sum+a;
```

```
        elseif k==0;
          a=0;
          sum=sum+a;
        else
          sum=sum+scrJ3(k);
        end
    end
     Intscr2(J)=sum;
end

%I create the image matrix for the Pyrophoric model
FOV=((pi*2)/180);
Range=1.8*(10^3); %(m)
Rfield=FOV*Range; %(m)
[r1,c1]=size(rnorm); % c1 takes the value of  size(r_max_t)
Cpf=zeros(Npix+1,Npix+1);
for i=-Npix/2:1:Npix/2;
    for j=-Npix/2:1:Npix/2;
       ipix=i+((Npix/2)+1);
       jpix=j+((Npix/2)+1);
       Nr=sqrt(i.^2+j.^2);
       R=(Rfield/(Npix+1))*Nr;
       L1=(R/(max(rnorm)*rmax))*c1;
       L=round(L1);
        if L>c1
           Cpf(ipix,jpix)=0;
        elseif L==0;
           Cpf(ipix,jpix)=0;
        else
           Cpf(ipix,jpix)=Intscr2(L);
       end
    end
end
Jts=Js*ratWfl;
sum=0;
for i=1:(Npix+1);
    for j=1:(Npix+1);
       sum= sum+ Cpf(i,j);
    end
end
newCpf= Cpf/sum *Jts;
Cpfn=newCpf;

               % ********* S/N Ratio *******
Ratio=Jplb/Jts

eval(['save data',num2str(z),'.mat']);
end

for z=1:length(tspf);
eval(['load data',num2str(z),'.mat']);
figure(z)
image(Cpfn,'CDataMapping','scaled')
end

figure(z+1)

image(Cpln,'CDataMapping','scaled')

end
```

Program 2 Plankpf.m

```
%  This function file calculates the Spectral Radiant Emittance (SRE)
%  for the pyrophoric at temperature Tpf(Kelvin).

function Y = plankpf(Lambda,T)
global Tpf
c1=3.7415e4;
c2=1.4388e4;
Y = c1 ./(Lambda .^5 .* (exp(c2 ./(Lambda .* Tpf))-1));
% Y will have units of watts/(cm^2-micron)
```

Program 3 Plankpl.m

```
%  This function file calculates the Spectral Radiant Emittance (SRE)
%  for the plume at temperature Tpl(Kelvin).

function Y = plankpl(Lambda,T)
global Tpl
c1=3.7415e4;
c2=1.4388e4;
Y = c1 ./(Lambda .^5 .* (exp(c2 ./(Lambda .* Tpl))-1));
% Y will have units of watts/(cm^2-micron)
```

Program 4 Dquad1.m

```
% DQUAD1     Numerically integrates an expression using QUAD8.

function [I]=dquad1(Fun,a1,a2,a3,a4)

var = 'x';
tol=1e-3;
if nargin<3,
help dquad1
return
end
if nargin == 3,
    xmin=a1;
    xmax=a2;
elseif nargin == 4,
   if (isstr(a1)),
    var=a1;
    xmin=a2;
    xmax=a3;
   else
    xmin=a1;
    xmax=a2;
    tol=a3;
   end
else
    var=a1;
    xmin=a2;
    xmax=a3;
    tol=a4;
end
I=quad8('plankpl',xmin,xmax,tol);
```

Program 5 Dquad2.m

```
% DQUAD2      Numerically integrates an expression using QUAD8.

function [I]=dquad2(Fun,a1,a2,a3,a4)

var = 'x';
tol=1e-3;
if nargin<3,
   help dquad2
   return
end
if nargin == 3,
    xmin=a1;
    xmax=a2;
elseif nargin == 4,
   if (isstr(a1)),
    var=a1;
    xmin=a2;
    xmax=a3;
   else
    xmin=a1;
    xmax=a2;
    tol=a3;
   end
else
    var=a1;
    xmin=a2;
    xmax=a3;
    tol=a4;
end
I=quad8('plankpf',xmin,xmax,tol);
```

Program 6 Gammaz.m

```
% GAMMAZ gamma function that also allows for complex arguments, unlike
%        MATLAB's GAMMA function. For real arguments, GAMMAZ gives the
%        same results as GAMMA (within numerical error).

function [f] = gammaz(z);

[m n] = size(z);
f = zeros(m,n);
cof = [76.18009172947146
      -86.50532032941677
       24.01409824083091
       -1.231739572450155
        0.1208650973866179e-2
       -0.5395239384953e-5];     % 6 coefficients in series expansion

for icol = 1:n,            % do one column at a time
  zz = z(:,icol);
  zp = ones(6,1)*zz' + [1:length(cof)]'*ones(1,length(zz)); % vectorize
  ser = (cof'*(1./zp)+1.000000000190015)';
  tmp = zz+5.5 - (zz+.5).*log(zz+5.5);
  lngamma = -tmp + log(2.5066282746310005*ser./zz);
  f(:,icol) = exp(lngamma);
end
```

APPENDIX C. MATHEMATICAL DERIVATIONS

1. Solution for t_p=a-1

The pdf of a standard Gamma RV is given by equation (III-7) in Chapter III. For convenience it is reproduced below

$$f(t;a)=\frac{1}{\Gamma(a)}t^{a-1}e^{-t} \qquad (C-1)$$

$$t \geq 0$$

$$a > 0$$

Now by setting

$$\frac{d}{dt}f(t,a)=0 \qquad (C-2)$$

$$with \quad \Gamma(a)=(a-1)!\neq 0 \quad for \quad a>0$$

we get

$$\frac{1}{\Gamma(a)}\left[(a-1)t^{a-2}e^{-t}+t^{a-1}\cdot(-1)e^{-t}\right]=0 \Rightarrow$$

$$\Rightarrow \left[(a-1)t^{a-2}e^{-t}+t^{a-1}\cdot(-1)e^{-t}\right]=0 \Rightarrow a=t+1 \qquad (C-3)$$

Now, for $t=t_p$

$$t_p = a-1 \qquad (C-4)$$

2. Positive side integration of Gaussian distribution

The pdf of a Gaussian RV is given by equation (III-10) in Chapter III. For convenience it is reproduced below

$$f(x;\mu,\sigma)=\frac{1}{\sqrt{2\cdot\pi}\cdot\sigma}\cdot e^{-(x-\mu)^2/2\cdot\sigma^2} \qquad \begin{array}{l} -\infty<x<\infty \\ -\infty<\mu<\infty \quad mean \\ 0<\sigma \quad standard \quad deviation \end{array} \qquad (C-5)$$

The above equation for μ=0 and σ=1 becomes

$$f(x;0,1)=\frac{1}{\sqrt{2\cdot\pi}}\cdot e^{-x^2/2} \qquad -\infty<x<\infty \qquad (C-6)$$

To find the area under the curve from x to infinity the following integral must be evaluated:

$$Q(x;0,1)=\frac{1}{\sqrt{2\cdot\pi}}\int_x^{\infty} e^{-y^2/2}\,dy \qquad (C-7)$$

In terms of the complementary error function

$$Q(x)=1/2\cdot erfc\left(x/\sqrt{2}\right) \qquad (C-8)$$

Now, if the continuous random variable X has mean μ and standard deviation σ then

$$Z = \frac{X - \mu}{\sigma} \qquad (C-9)$$

is a Gaussian random variable with $\mu=0$ and $\sigma=1$, and the area under the curve from z to infinity is

$$Q(z;0,1) = \frac{1}{\sqrt{2 \cdot \pi}} \int_z^{\infty} e^{-y^2/2} dy \qquad (C-10)$$

From equation (C-8), we have

$$Q(z) = \frac{1}{2} \cdot erfc\left(\frac{z}{\sqrt{2}}\right) \qquad (C-11)$$

The area under the curve from zero to infinity is obtained by setting x=0 in the previous equation to obtain [5]

$$Q(z) = \frac{1}{2} \cdot erfc\left(\frac{-\mu}{\sigma \cdot \sqrt{2}}\right) \qquad (C-12)$$

LIST OF REFERENCES

[1] Richard D.Hudson,*Infrared System Engineering*,John Wiley&Sons,1969

[2] John P.Powers,*An Introduction to Electro-Optic Systems*,Department of Electrical and Computer Engineering Naval Postgraduate School,1998

[3] Accetta Shumaker,*The Infrared & Electro-Optical Systems Handbook*,Vol 2,Infrared Information Analysis Center,1996

[4] Accetta Shumaker,*The Infrared & Electro-Optical Systems Handbook*,Vol 7,Infrared Information Analysis Center,1996

[5] Jay L.Devore,*Probability and Statistics for Engineering and the Sciences*,Brooks/Code Publishing Company,1995

INITIAL DISTRIBUTION LIST

No.Copies

1. Defense Technical Information Center 2
   8725 John J.Kingnan Road, Ste 0944
   Fort Belvoir, VA 22060-6218

2. Dudley Knox Library 2
   Naval Postgraduate School
   411 Dyer Road
   Monterey, California 93943-5101

3. Chairman, Code EC 1
   Department of Electrical and Computer Engineering
   Naval Postgraduate School
   Monterey, California 93943-5121

4. Professor R.Pieper, Code EC/Pr 2
   Department of Electrical and Computer Engineering
   Naval Postgraduate School
   833 Dyer Road, Room 437
   Monterey, California 93943-5121

5. Professor R.C.Robertson, Code EC/Rc 2
   Department of Electrical and Computer Engineering
   Naval Postgraduate School
   833 Dyer Road, Room 437
   Monterey, California 93943-5121

6. Program Executive Officer 1
   Tactical Aircraft Programs (PMA-272F/E2)
   Attn: CDR Joel Sewell
   Building 2272/Suite 535 NAVAIRSYSCOM HQ
   47123 Buse Road Unit IPT
   Patuxent River, MD 20670-1547

7. Commander(Code 4072) 1
   NAVSURWARCENDIV
   Attn:Norm Papke
   300 Highway 361
   Crane, IN 47522-5001

8. Commander 1
   Naval Air Warfare Center Aircraft Division
   Attn:Chip Guffey (4.11.9C)
   Bldg.2109 Suite S246
   48150 Shaw Road Unit 5
   Patuxent River, MD 20670-1907

9. Mike Veracka 1
Naval Research Lab
Code 5711
4555 Overlook Ave, SW
Washington, D.C. 20375-5339

10. Mihail Demestihas 2
Anastaseos 126 Papagos
Athens, GREECE